

Interaction between low-level jets and wind farms in a stable atmospheric boundary layer

Srinidhi N. Gadde* and R. J. A. M. Stevens

*Physics of Fluids Group, Max Planck Center Twente for Complex Fluid Dynamics,
J. M. Burgers Center for Fluid Dynamics and MESA+ Research Institute,
University of Twente, P. O. Box 217, 7500 AE Enschede, The Netherlands*

(Dated: July 29, 2021)

Low-level jets (LLJs) are the wind maxima in the lower regions of the atmosphere. The momentum in the LLJs can serve as a source of high capacity energy for wind turbines. In this work, large-eddy simulations are used to study the effect of LLJs and low-lying temperature inversions on the power production of wind farms by systematically increasing the stability of the boundary layer. We vary the LLJ height and study the development of the internal boundary layer and the change in the wind farm power production. We observe that the turbulence intensity decreases with increasing stratification and LLJs with a pronounced wind maximum develop to sustain continuous turbulence. Flow visualization reveals that the low-lying capping inversion limits the growth of the wind farm internal boundary layer and forces the wind to go around the wind farm. This effect is stronger at higher stratification; i.e. more wind goes around the wind farm. However, when the stratification is weak the flow prefers going over the wind farm.

We find that the height of the LLJ determines the wake recovery and power production in the wind farm. When the jets are far above the wind turbines, higher entrainment in the rear of the wind farm causes an increase in power production. If the jets are at the same height as the top of the wind turbines, the turbine wakes can directly interact with jet via meandering. Furthermore, in the case of very low jet heights, the energy in the jet is completely extracted by the row of turbines at the entrance with which LLJ directly interacts. Wind turbines extract energy, and the jet is destroyed in the downstream direction as it passes through consecutive turbine rows. An energy budget analysis is carried out to analyze the effect of different flow phenomena on the wind farm power production. The budget analysis shows elevated entrainment rates in the presence of LLJs, emphasizing the effect of jets as an additional momentum source. At high stratification, the combined effect of buoyancy destruction and turbulence dissipation is more than the turbulent entrainment, and causes a slower wake recovery.

The wind veer introduced by the Coriolis force creates a spanwise flow causing an asymmetry in the wind availability for different turbine columns. In the presence of a LLJ the turbines that can directly extract energy from the LLJ produce the most power. The reason is that the turbines at the entrance of the wind farm destroy the jet due to which turbines further downstream cannot benefit from the LLJ. However, while the turbines at the entrance of the wind farm can be subjected to strong shears, the turbines further downstream are not. We find that the characteristics of the incoming atmospheric flow wind determine the performance of the turbines at the entrance of the wind farm. However, the performance of turbines further downstream is determined by the vertical entrainment of kinetic energy, which is created by the turbulent fluxes.

I. INTRODUCTION

The atmospheric boundary layer is dynamic and undergoes continuous transitions during the day due to the changes in forcing, such as the surface heat flux and the geostrophic wind. During the evening boundary-layer transition with cooling at the ground, the flow above the surface layer decouples from the surface friction. Consequently, the balance between the Coriolis, frictional, and pressure forces is disturbed, and the flow above the surface layer accelerates. The acceleration produces a super-geostrophic jet at the top of the nocturnal stable boundary layer (SBL) at low heights (50 – 1000 m) of the atmosphere [1]. This super-geostrophic wind is called the low-level jet (LLJ), and it generally forms due to the aforementioned frictional decoupling combined with inertial oscillations [2, 3]. Additionally, a LLJ can also form due to large-scale baroclinicity or the pressure gradient due to cooling over sloped terrains [4]. In general, LLJs form in nocturnal conditions when there is surface cooling. Mahrt (1998) [5] classified the nocturnal

*Electronic address: s.nagaradagadde@utwente.nl; Physics of Fluids Group, Max Planck Center Twente for Complex Fluid Dynamics, J. M. Burgers Center for Fluid Dynamics and MESA+ Research Institute, University of Twente, P. O. Box 217, 7500 AE Enschede, The Netherlands

boundary layer into three stability regimes: 1) the weakly stable regime, characterized by continuous turbulence and a small downward heat flux, which is limited by the temperature fluctuations, 2) transition stability regime, where the quantities change rapidly with the increasing stability and the downward heat flux reaches a maximum, and 3) the very stable regime where the downward heat flux is small, limited by the turbulent vertical fluctuations, which are suppressed by buoyancy. LLJs of practical importance are characterized by high shear and weak to moderate stability [6, 7]. The shear in the LLJ is strong enough to generate continuous turbulence with maximum and minimum values at the surface and top of the SBL, respectively [5].

LLJs are frequently observed in many parts of the world, with occurrences in the Western ghats of India [8], the Great Plains of the United States [9–11], the North sea, and the Baltic sea of Europe [12, 13]. LLJs have wide-ranging impact in the atmosphere, the wind shear in a LLJ can cause dangerous deviations from the nominal glide path of an aircraft resulting in a premature touch-down [14], the high-speed jet can increase the dispersion and transport of pollutants in the atmosphere [15], and a LLJ formed in the upper layers of the atmosphere can even impact bird migrations [16]. Furthermore, LLJs have a direct impact on wind energy based power production [17]. It is a common practice in wind power assessment to use simple, power-law velocity profiles. However, this overlooks the high power density and strong shears associated with a LLJ phenomenon. This results in an underestimation of both power production and the fatigue loads on the wind turbine [18]. LLJs have been found to increase the capacity factors by over 60% under nocturnal conditions [19]. Present-day wind turbines are reaching heights above 200 m due to which interactions with LLJs becomes unavoidable. Consequently, it is imperative to study the interaction between LLJs and wind farms.

When a large number of wind turbines operate in a wind farm, the structure of the boundary layer changes due to the momentum extraction by the turbines. Both numerical simulations and wind tunnel experiments show the development of an internal boundary layer (IBL) at the entrance of the wind farm [20–22]. Further downstream, in the fully developed regime, all the momentum is derived from vertical entrainment [23, 24]. Owing to the simplicity, most wind farm and atmospheric boundary layer simulations in the past have focused on pressure-driven neutral boundary layers. The underlying assumption in such simulations is that the wind turbines reside in the inner regions of the atmospheric boundary layer, where the outer layer effects such as the rotation of the Earth and thermal stratification are negligible [23, 25]. However, the wake recovery and entrainment of fresh momentum from outside the IBL are heavily dependent on the turbulence intensity, which in turn depends on the stratification in the atmosphere [26, 27]. Furthermore, the wind follows an Ekman spiral due to the Coriolis force and causes a wind veer affecting the turbine wakes as well as the combined wind farm wake. In essence, neglecting the stratification and Coriolis forces is too simplistic when large wind farms are considered.

Large-eddy simulation (LES) technique has been used extensively to study turbulence in the atmosphere [28, 29], and the interaction between the atmospheric boundary layer and wind farms [25, 30, 31]. LES has been successfully used to simulate both convective and stable atmospheric boundary layers at both weak and moderate stratification [32–36]. Numerical simulations of weak and moderately stratified SBL are easier because of the continuous turbulence and the absence of global intermittency [37]. The simulations of highly stratified boundary layers are challenging due to the mesoscale motions, gravity waves, the unsteady nature of the boundary layers, and LLJs. Nocturnal LLJs under weak to moderate stratification have been extensively studied with LES [36, 38].

Recently, the impact of the capping inversion on the power production of ‘infinitely’ wide wind farms in conventionally neutral boundary layers is reported in the literature [39]. It is found that the IBL pushes the capping inversion upwards, which generates pressure perturbations that travel upstream as gravity waves and slow down the upstream wind. Furthermore, studies of wind farms in a neutral-to-stable boundary layer transition and they note that in a steady-state SBL the LLJ impact the power production [40]. Also, measurements and LES studies of wind farms in SBL [27, 40–42] show that due to low turbulence intensity, wake recovery is reduced compared to the unstable and neutrally stratified boundary layer. In addition, the rotation of the Earth affects the power production with the Coriolis force rotating the wind farm wake [43]. For certain wind directions it has been found that even the horizontal component of the Earth’s rotation influences the turbulent fluxes in a wind farm [44]. Furthermore, the vertical wind veer in the Ekman spiral causes a skewed spatial structure of the turbine wake and also enhances shear production of turbulent kinetic energy leading to larger flow entrainment and thus faster wake recovery [45]. It is a common practice in the wind energy community to use periodic boundary conditions in the spanwise direction, which results in ‘infinitely’ wide wind farms [23, 30, 46, 47]. However, in the presence of Coriolis force, which induces appreciable spanwise flow, this assumption might lead to under-prediction of power in the turbine columns which directly interact with the LLJ.

Previously, wind turbine and LLJ interactions have been studied by Lu and Porté-Agel (2011) [48], who performed LES of the flow over a turbine in a doubly periodic domain (an ‘infinite’ wind turbine array) with actuator line modeling, and they report non-axisymmetric turbine wakes and LLJ elimination due to energy extraction by the turbines. A similar study of the interaction between a single turbine and LLJ reports slower wake recovery at higher stratification and LLJ elimination [49]. Furthermore, the LLJ weakening due to the extraction of momentum by

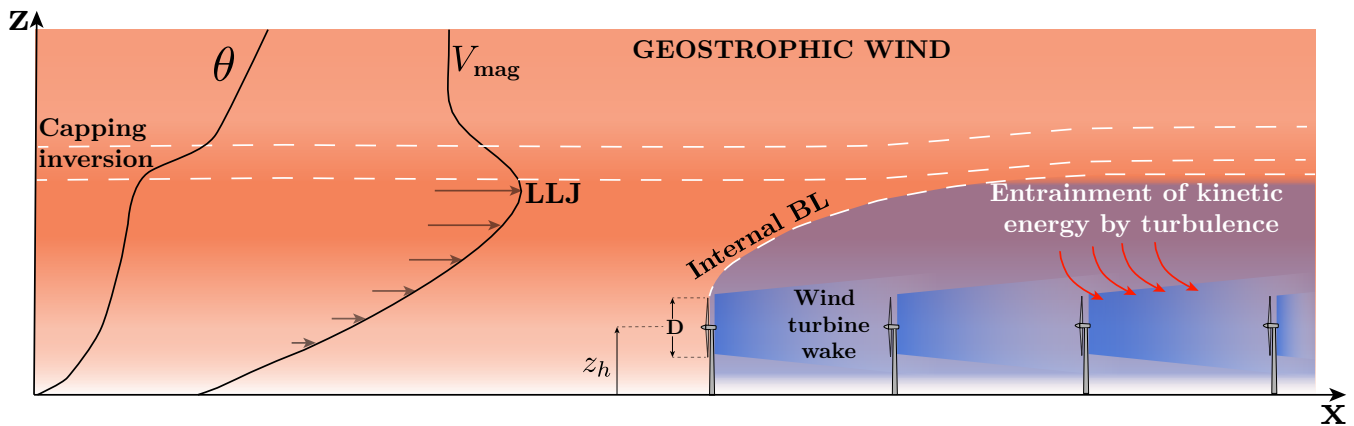


FIG. 1: Sketch of the essential flow phenomena in wind farms in a SBL, including wakes and their superposition, the entrainment of momentum from above, and the development of the IBL. On the left, the typical temperature and velocity profiles, which reveal the LLJ and the capping inversion, are sketched.

the turbines is also reported in wind farm simulations in which the diurnal cycle is considered [50, 51]. A similar phenomenon has been observed in the mesoscale weather model simulations of an infinite wind farm [52]. Recently, Na et al. [53] performed LES of a small wind farm with 12 turbines arranged in 3 columns and 4 rows with a LLJ above it in a spanwise periodic domain. They report faster wake recovery due to the enhanced vertical kinetic energy flux created by the LLJ.

The studies mentioned above have not addressed the effect of changing LLJ height on wind farm power production. Furthermore, the previous studies do not provide a complete picture of the interaction between LLJs and wind farms, either because of the ‘infinite’ wind farm assumption, or the spanwise periodic small size wind farms. The assumptions are not applicable for a fully finite wind farm. The flow is further complicated by interaction between the low-lying capping inversion and the wind farm IBL. It is necessary to understand the coupling between stable stratification, flow-adjustment, and LLJ height on wind farm power production. Figure 1 shows the essential flow phenomena such as the IBL growth, turbine wake recovery, modification of the capping inversion, and the entrainment of momentum from above by turbulence.

In this work, we study the effect of LLJs in stable stratification in a finite wind farm with no periodicity along the boundaries by systematically varying the surface cooling rate which results in changing LLJ heights. The objective of the study is two-fold, first to study the effect of LLJ height and stable stratification on the power production of a wind farm, and second to study the effect of low-lying capping inversions on the flow adjustment in and around a ‘finite’ wind farm.

The remainder of the paper is structured as follows, in section II, the LES and numerical method are detailed. In section III important boundary layer properties, the IBL growth above the wind farm, and the flow adjustment around the wind farm are discussed. In section IV, an analysis of the different flow phenomena is carried out by performing an energy budget analysis. Furthermore, in section V, the effect due to the wind veer is discussed, which is followed by the conclusions in section VI.

II. LARGE-EDDY SIMULATIONS

In LES, the flow features larger than the filter size are fully resolved, while the sub-filter size eddies are modeled. Our code is an updated version of the one used by [23, 54]. This updated code has been validated for neutral and SBLs as well as the flow-through wind farms [55–57]. The governing equations and numerical method are discussed in section II A, and the boundary layer initialization is explained in section II B, followed by the wind farm setup in section II C.

A. Governing equations and numerical method

The LES code we use integrates the filtered Navier-Stokes equations written for a wall-bounded turbulent flow [58] and employs the Boussinesq approximation to model buoyancy. The governing equations are:

$$\partial_i \tilde{u}_i = 0, \quad (1)$$

$$\begin{aligned} \partial_t \tilde{u}_i + \partial_j (\tilde{u}_i \tilde{u}_j) = & -\partial_i \tilde{p} - \partial_j \tau_{ij} + g\beta(\tilde{\theta} - \tilde{\theta}_0)\delta_{i3} + f_c(U_g - \tilde{u})\delta_{i2} \\ & - f_c(V_g - \tilde{v})\delta_{i1} + \tilde{f}_x\delta_{i1} + \tilde{f}_y\delta_{i2}, \end{aligned} \quad (2)$$

$$\partial_t \tilde{\theta} + \tilde{u}_j \partial_j \tilde{\theta} = -\partial_j q_j, \quad (3)$$

where, the tilde represents spatial filtering, $\tilde{u}_i = (\tilde{u}, \tilde{v}, \tilde{w})$ and $\tilde{\theta}$ are the filtered velocity and potential temperature, respectively, g is the acceleration due to gravity, $\beta = 1/\theta_0$ is the buoyancy parameter with respect to the reference potential temperature θ_0 , δ_{ij} is the Kronecker delta, f_c is the Coriolis parameter. The boundary layer is driven by a mean pressure gradient, p_∞ , represented by the geostrophic wind with, $U_g = -\frac{1}{\rho f_c} \frac{\partial p_\infty}{\partial y}$ and $V_g = \frac{1}{\rho f_c} \frac{\partial p_\infty}{\partial x}$ as its components. $\tilde{p} = \tilde{p}^*/\rho + \sigma_{kk}/3$, is the modified pressure obtained by adding the trace of the sub-filter scale stress, $\sigma_{kk}/3$, to the kinematic pressure or pressure perturbation, \tilde{p}^*/ρ , where ρ is the density of the fluid. $\tilde{f}_i = (\tilde{f}_x, \tilde{f}_y, 0)$ represents the turbine forces, which are modeled using a filtered actuator disk approach [23, 59, 60]. The molecular viscosity is neglected as it is a high Reynolds number flow, which is a common practice in atmospheric boundary layer simulations. $\tau_{ij} = \tilde{u}_i \tilde{u}_j - \tilde{u}_i \tilde{u}_j$ is the traceless part of the sub-filter scale stress tensor, and $q_j = \tilde{u}_j \tilde{\theta} - \tilde{u}_j \tilde{\theta}$ is the sub-filter scale heat flux tensor. The sub-filter stresses and heat fluxes are modeled as,

$$\tau_{ij} = \tilde{u}_i \tilde{u}_j - \tilde{u}_i \tilde{u}_j = -2\nu_T \tilde{S}_{ij} = -2(C_s \Delta)^2 |\tilde{S}| \tilde{S}_{ij}, \quad (4)$$

$$q_j = \tilde{u}_j \tilde{\theta} - \tilde{u}_j \tilde{\theta} = -\nu_\theta \partial_j \tilde{\theta} = -(D_s \Delta)^2 |\tilde{S}| \partial_j \tilde{\theta}, \quad (5)$$

where, $\tilde{S}_{ij} = \frac{1}{2} (\partial_j \tilde{u}_i + \partial_i \tilde{u}_j)$ is the filtered strain rate tensor, ν_T is the eddy viscosity, C_s is the Smagorinsky coefficient for the sub-filter stresses, Δ is the filter size, ν_θ is the eddy heat diffusivity, D_s is the Smagorinsky coefficient for the sub-filter scale heat flux, and $|\tilde{S}| = \sqrt{2\tilde{S}_{ij}\tilde{S}_{ij}}$. We use a tuning-free, scale-dependent model based on Lagrangian averaging of the coefficients [61–63] to dynamically calculate the Smagorinsky coefficient. The error in the calculation of the Smagorinsky coefficients is minimized over fluid pathlines preserving the local fluctuations of the coefficients. This makes the model particularly suitable for inhomogeneous flows, such as the flow through a wind farm or over complex terrain.

We use a pseudo-spectral method to calculate the partial derivatives in the streamwise and spanwise directions. The vertical direction is treated with a second-order central difference method. The solution is advanced in time by a second-order accurate Adams-Bashforth scheme. The aliasing errors resulting from the folding back of high wavenumber energy to the resolved scales due to the calculation of non-linear terms in physical space is prevented by using a 3/2 anti-aliasing method [64]. For pointwise energy conservation, the convective term in the equation 2 is written in the rotational form [65]. More information about the numerical method can be found in [58]. The computational domain is discretized uniformly with n_x , n_y , and n_z points in the streamwise, spanwise, and vertical directions, respectively. Therefore, the corresponding grid sizes are $\Delta_x = L_x/n_x$, $\Delta_y = L_y/n_y$, and $\Delta_z = L_z/n_z$, where L_x , L_y , and L_z are the dimensions of the computational domain. The computational grid is staggered in the vertical direction with the first grid point for \tilde{u}, \tilde{v} , and $\tilde{\theta}$ located at a distance $\Delta_z/2$ above the ground. The computational plane for the vertical velocity, \tilde{w} , is located at the ground. No-slip and free-slip boundary conditions with zero vertical velocity, $\tilde{w} = 0$, are used at the top and bottom boundaries, respectively. In wall-modeled LES of atmospheric boundary layers, the first grid point generally lies in the surface layer and the Monin-Obukhov similarity theory [28] can be used to model the instantaneous shear stress $\tau_{i3|w}$ and buoyancy flux q_* at the wall as follows

$$\tau_{i3|w} = -u_*^2 \frac{\tilde{u}_i}{\tilde{u}_r} = -\left(\frac{\tilde{u}_r \kappa}{\ln(z/z_o) - \psi_M} \right)^2 \frac{\tilde{u}_i}{\tilde{u}_r}, \quad (6)$$

and

$$q_* = \frac{u_* \kappa (\theta_s - \tilde{\theta})}{\ln(z/z_o) - \psi_H}, \quad (7)$$

where \tilde{u}_i and $\tilde{\theta}$ represents the filtered velocities and potential temperature at the first grid point respectively, u_* is the frictional velocity, z_o is the roughness length, κ is the von Kármán constant, $\tilde{u}_r = \sqrt{\tilde{u}^2 + \tilde{v}^2}$ is filtered velocity

magnitude at the first grid level, and θ_s is the filtered potential temperature at the surface. ψ_M and ψ_H are the stability corrections for momentum and heat flux, respectively. For SBLs, we use the stability correction suggested by [38], i.e. $\psi_M = -4.8z/L$ and $\psi_H = -7.8z/L$, where $L = -(u_*^3 \theta_0)/(\kappa g q_*)$ is the surface Obukhov length.

B. Boundary layer initialization

Simulating strongly stratified boundary layers with LES is complicated due to the presence of globally intermittent turbulence [37]. In the present work, we consider a moderate stratification ($z_i/L \approx 2$, where z_i is the boundary layer height), which remains continuously turbulent. The boundary layer represents a typical quasi-equilibrium moderately SBL with a pronounced LLJ similar to those observed over polar regions and equilibrium night-time conditions over land in mid-latitudes. The case is well-documented under the global energy and water cycle experiment atmospheric boundary layer study (GABLS-1) initiative and LES inter-comparison studies [36, 38]. The initial potential temperature profile has a mixed layer (with constant potential temperature 265 K) up to 100 m with an overlying free atmospheric stratification of strength 0.01 Km^{-1} . The reference potential temperature and roughness length are set to 263.5 K and 0.1 m, respectively, and a constant surface cooling is applied. The boundary layer is driven by the geostrophic wind with the horizontal components $G = (U_g, V_g) = (8.0, 0.0) \text{ ms}^{-1}$. The Coriolis parameter is set to $f_c = 1.39 \times 10^{-4} \text{ s}^{-1}$ (corresponding to latitude 73°N). The initial wind profile is set equal to the geostrophic wind. To spin up turbulence, uniformly distributed random perturbations with an amplitude of 3% of the geostrophic wind are added to velocities below a height of 50 m. Similarly, uniformly distributed random perturbations with a magnitude of 0.1 K are added to the initial temperature profile. Detailed information about the SBL can be found in [38].

The boundary layer reaches a quasi-steady state at the end of 8th hour. The quasi-steady-state is said to have been reached when the temperature profile changes at a constant rate while the velocity and other turbulent quantities have reached a steady-state [36]. Our code has been validated for the GABLS-1 boundary layer with a cooling rate of $0.25 \text{ K} \cdot \text{hour}^{-1}$. In agreement with the previous study by Stoll and Porté-Agel (2008) [63], we found that the Lagrangian averaged scale-dependent (LASD) model produces better results when compared with the Smagorinsky model. We performed five simulations with surface cooling rates $C_r = [0.0, 0.125, 0.25, 0.375, 0.5] \text{ K} \cdot \text{hour}^{-1}$. Details about the different cases are documented in table I.

C. Wind farm setup

We consider a large wind farm with 40 wind turbines. The turbines are distributed in an array of 4 columns and 10 rows. The turbine diameter is $D = 90 \text{ m}$ and the hub height is $z_h = 90 \text{ m}$. The turbines are separated by a distance of $s_x = 7D$ and $s_y = 5D$ in the streamwise and spanwise directions, respectively. The computational domain is $11.52 \text{ km} \times 4.6 \text{ km} \times 3.84 \text{ km}$. The details of the computational domain and wind farm layout are given in figure 2. According to the Monin-Obukhov similarity theory first grid point above the ground should be in the inertial sublayer. For the GABLS-1 case, cautioning against using very high resolution near the ground which violates the similarity theory, Basu and Lacser (2017) [66] prescribe a guideline of $z_1 \geq 50z_o$, where z_1 the height of the first grid point above the ground. Accordingly, we fix the vertical grid resolution to be 5 m. We use a horizontal resolution of 9 m in the streamwise and spanwise direction to ensure that all important flow scales are properly resolved. As a result the domain is discretized by $1280 \times 512 \times 768$ grid points in the streamwise, spanwise, and vertical directions, respectively. The computational domain has approximately 500 million grid points.

We use a large vertical extent and a Rayleigh damping layer [67] with a strength of 0.016 s^{-1} in the top 25% of the domain to reduce the effects of gravity waves. It was found that this damps out most gravity waves that are generated. To ensure that the streamwise fringe layer does not affect the turbulence statistics, we performed a simulation in a bigger domain of size $17.28 \text{ km} \times 4.6 \text{ km} \times 3.84 \text{ km}$ with a resolution of $18 \text{ m} \times 18 \text{ m} \times 10 \text{ m}$ and compared it with the results of the smaller domain. The streamwise fringe layer in the bigger domain is at a distance $75D$ away from the wind farm. We found that the streamwise domain size does not affect the turbulence statistics relevant to the study, which confirms that the used domain size is reasonable.

To obtain realistic inflow conditions, we employ the concurrent precursor technique [68]. In this technique, simulations are run in two domains concurrently. In the precursor domain, we perform the atmospheric boundary layer simulations without wind turbines to generate inflow conditions, and then the quantities from the precursor domain are used as the inlet conditions for the wind farm domain. The forcing is done in the wind farm domain by gradually blending the velocities in the fringe layer. Due to the Coriolis forces an Ekman spiral, which induces considerable spanwise flow, is formed. Therefore, we use fringe layers in both the streamwise and spanwise direction to eliminate the effects of the periodic boundaries. We fix the fringe layer length to be 10% of the computational domain in the

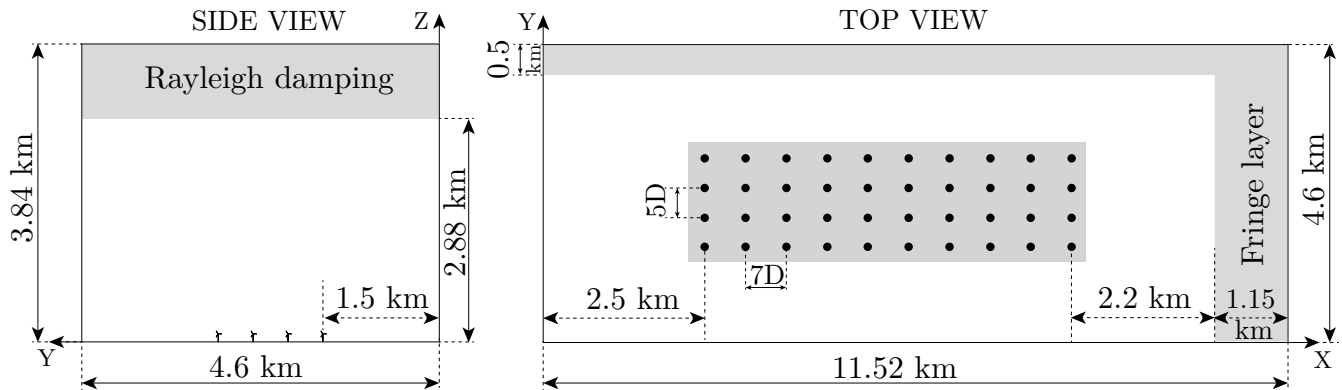


FIG. 2: Schematic showing the extent of Rayleigh damping layer, the fringe layers, and the wind farm layout. Black circles indicate the positions of the wind turbines. The statistics are sampled from the shaded region of size $70D \times 20D \times D$, which is centered around the wind farm.

Case	C_r [$\text{K} \cdot \text{h}^{-1}$]	z_i/z_h	z_{jet}/z_h	z_c/z_h	u_*/G	u_{jet}/G	z_i/L	TI_{z_h} %
SBL-1	0.000	2.839	2.670	3.023	0.0395	1.109	0.350	5.62
SBL-2	0.125	2.313	2.169	2.506	0.0348	1.157	1.103	4.29
SBL-3	0.250	1.903	1.836	2.114	0.0316	1.180	1.713	3.18
SBL-4	0.375	1.668	1.557	1.840	0.0296	1.187	2.274	2.40
SBL-5	0.500	1.551	1.446	1.639	0.0285	1.189	2.859	1.95

TABLE I: Details of the simulations presented in this study. The columns from left to right indicate the case name, the surface cooling rate C_r , the boundary layer height z_i , the jet height z_{jet} , and the capping inversion height z_c . u_{jet} is the velocity at jet height. $TI = \sigma_u/u_{\text{mag}}$ is the turbulence intensity at hub height. Note that all heights are normalized with the hub height.

streamwise and spanwise directions, respectively.

The equilibrium wind angle under geostrophic forcing depends on the stability conditions, which results in a different geometric pattern of the turbines and complicates the analysis. To ensure the same farm layout in all simulations, we use a proportional-integral (PI) controller [69], similar to the one used by [46], to rotate the incoming flow such that the planar averaged wind angle at hub height is always zero. Even then, local changes in the wind angle upstream of a turbine can result in turbine yaw misalignment, which results in sub-optimal energy production. To prevent this, each turbine in the simulations has an individual yaw-angle controller, which reorients the orientation of the turbines such that it is perpendicular to the local wind angle measured $1D$ upstream of each turbine.

III. LES OF A FINITE WIND FARM

All the simulations are carried out in two stages. In the initial or the spin-up stage only the SBL in the precursor domain is considered. The SBL reaches quasi-steady state at the end of the 8th hour. In the second stage, the turbines are introduced in the main domain, and the simulation in both domains are continued concurrently for one more hour in which the transient effects of the turbine startup subside. Finally, both simulations are run for one more hour, and the statistics are collected in the last hour i.e. the 10th hour. The one-hour statistics was collected in six ten minute samples to quantify the uncertainty in the mean values. The standard deviation over the mean is found to be within 5% for all the equilibrium profiles. In the following sections, the basic boundary layer properties are presented in section III A, and the development of the IBL over the wind farm and the flow-adjustment are discussed in section III B.

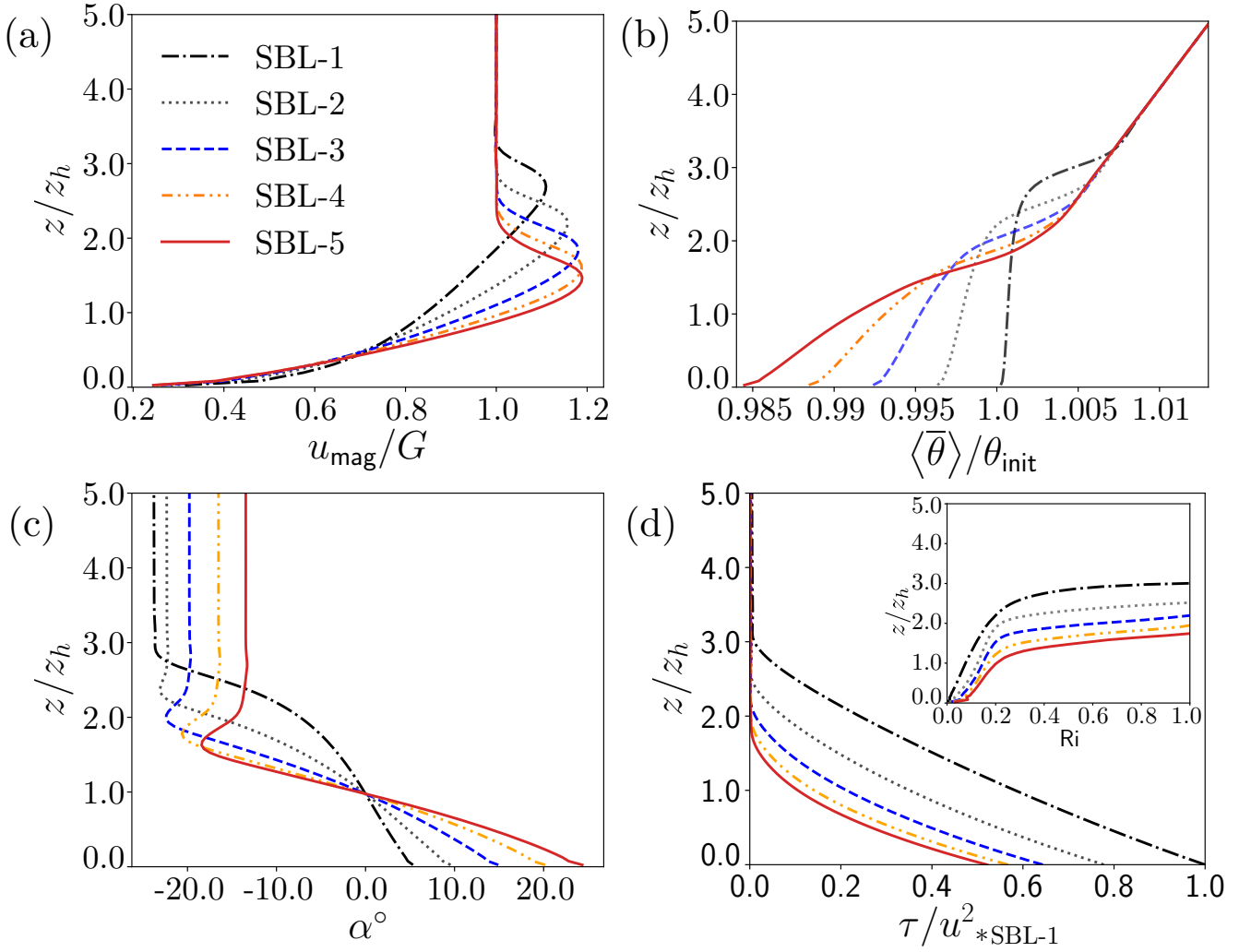


FIG. 3: The (a) horizontal velocity magnitude, (b) potential temperature, (c) wind angle, and (d) vertical momentum as a function of height for the different cases, see table I for details. The inset in panel (d) shows the variation of the gradient Richardson number with height.

A. Boundary layer properties

An overview of the surface forcings and the basic boundary layer properties such as the boundary layer height, friction velocity, jet velocity, and the stability parameter z_i/L in the precursor domain, are presented in table I. We determine the boundary layer height by the method used by [36] and [38]. The boundary layer height z_i is defined as the height where the mean stress is 5% of its surface value ($z_{0.05}$) followed by a linear extrapolation, i.e., $z_i = z_{0.05}/0.95$. At higher cooling rates, the friction velocity decreases, which indicates that there is a reduced turbulence in the boundary layer. Furthermore, the boundary layer becomes shallower, i.e. z_i reduces.

Figure 3(a) presents the planar averaged horizontal wind magnitude $u_{\text{mag}} = \langle \sqrt{\tilde{u}^2 + \tilde{v}^2} \rangle$, where $\langle \rangle$ represents planar averaging, the overbar represents time averaging, and the tilde representing filtering is dropped in rest of the paper for simplicity. The strength of the jet, which is defined as the ratio of wind magnitude of the jet to the geostrophic velocity, i.e., u_{jet}/G , increases as the cooling rate increases while the jet height z_{jet}/z_h decreases. The jet plays an important role in sustaining continuous turbulence in the boundary layer [5, 7]. For stronger stratification cases SBL-4 and SBL-5 (see table I), the height of the jet relative to the turbine hub height is approximately 1.5, which means that the jet height is equal to the height of the top of the turbine blades.

Figure 3(b) shows the planar averaged potential temperature profile. The height of the capping inversion z_c is defined as the height where the temperature gradient is maximum. For $z_c/z_h \leq 1.8$, we observe that the inversion height is approximately equal to the SBL height, such that the direct interaction with the IBL developed by the wind

farm is possible. Figure 3(c) presents the wind angle variation α as a function of height for the different cases. For higher cooling rates, a wind veer as strong as $15^\circ - 20^\circ$ is observed.

Based on z_i/L , Holtslag and Nieuwstadt (1986) [70] identified three SBLs regimes, namely 1) near-neutral regime ($0 < z_i/L \leq 1$) with weak stability characterized by continuous turbulence, 2) an intermediate regime ($1 < z_i/L \leq 10$) with moderate stability where the boundary layer follows z-less scaling with continuous turbulence, and 3) a highly stable intermittency regime ($z_i/L > 10$) where the turbulence is weak and sporadic and therefore not continuous in time and space. In all the cases considered in the present study, $z_i/L < 3$, indicating weak to moderate stability of the boundary layers. The boundary layer under such conditions remains continuously turbulent, and the similarity theory applies to the surface layer. Furthermore, continuous turbulence is sustained by the high shear of the LLJs.

In addition to z_i/L the effect of capping inversion, which takes into account the free atmospheric stratification, can also be characterized by the gradient Richardson number (Ri) calculated by the Brunt-Väisälä frequency N and mechanical shear S :

$$\text{Ri}(z) = \frac{N^2}{S^2}; \quad N^2 = \frac{g}{\theta_0} \frac{\partial \langle \bar{\theta} \rangle}{\partial z}; \quad S^2 = \left[\left(\frac{\partial \langle \bar{u} \rangle}{\partial z} \right)^2 + \left(\frac{\partial \langle \bar{v} \rangle}{\partial z} \right)^2 \right]. \quad (8)$$

Figure 3(d) shows the planar averaged vertical momentum flux in the precursor domain. The planar averaged vertical momentum flux defined as $\tau = \left\langle \sqrt{(u'w')^2 + (v'w')^2} \right\rangle$, where $\overline{u'w'} = \left(\overline{uw} + \overline{\tau_{xz}} \right) - \bar{u} \bar{w}$, and $\overline{v'w'} = \left(\overline{vw} + \overline{\tau_{yz}} \right) - \bar{v} \bar{w}$. The fluxes are normalized with the surface flux of the SBL-1 case to show the reduction in the turbulent momentum flux at higher cooling rates. It is evident from figure 3(d) that the turbulence in the boundary layer reduces when the surface cooling rate is increased. The inset in figure 3(d) shows that the Richardson number Ri increases monotonically with height for all the cases. At the top 10-20% of the boundary layer, the Ri increases above the critical Ri_c (based on the hydrodynamic instability theory [71–74]).

Zilitinkevich et al. [75] classify the boundary layer into three regimes: 1) weakly stable regime at $\text{Ri} < 0.1$, 2) a transitional regime at $0.1 \leq \text{Ri} \leq 1$ with strong turbulence at $\text{Ri} \ll 1$; and 3) weak turbulence regime at $\text{Ri} > 1$, capable of transporting momentum but not heat. At higher cooling rates (cases SBL-4 and SBL-5), the Ri number increases rapidly with height, limiting the turbulence to very low heights, which affects the IBL dynamics in the presence of a wind farm.

To conclude, the initialization stage yields completely turbulent, quasi-steady boundary layer which serves as an realistic inflow condition for the wind farm.

B. Flow adjustment in and around the wind farm

Instantaneous flow structures of the horizontal velocity for the SBL-3 case are shown in figure 4. The top panel shows the velocity contours in an x-z plane (through the 3rd column, note that only the lowest $z/D = 5$ is shown). We observe significant wake meandering in the vertical direction and that the boundary layer turbulence is restricted to the region below the capping inversion. The meandering of the wakes in the vertical direction can play a significant role in entraining the high-velocity fluid in the jet. The figure shows that the turbine wakes interact directly with the LLJ, inducing mixing, and reducing the strength of the jet. Besides, we note that the LLJ is reduced in intensity after the 5th row of the wind farm. Due to strong stratification and low lying inversion, the turbulence is more or less limited to the small region above the wind farm. The middle panel of figure 4 shows a horizontal snapshot of the flow at hub height (x-y plane). We notice significant wake meandering in the lateral direction and significant turbulence in the rear of the wind farm. In contrast with a neutral boundary layer with alternating high and low-speed turbulent streaks, the boundary layer, in this case, is only composed of small scale turbulent structures. Finally, the bottom panel shows a y-z plane at a distance (1D) behind the 6th turbine row. This figure is interesting as it shows a significant spanwise flow of the fluid with the LLJ impinging on the turbine in the 1st column on the left. This happens due to the wind veer induced by the Coriolis forces and is discussed in section V. As a result, the turbines in the 1st column entrain the high-velocity jet, which increases the power production. Another noteworthy point here is that the figure shows the importance of performing non-periodic, fully-finite simulations with a fringe layer in the spanwise direction. If a spanwise fringe layer is not used for the inlet, the turbine in the 1st column would be operating in the wake of the wind farm, consequently under-predicting the turbine power output.

The turbines extract energy from the incoming flow and thereby create a momentum deficit in the wake. The wakes start interacting with the boundary layer both in the lateral and vertical direction via turbulence, and the momentum deficit spreads in the boundary layer, which in turn entrains air towards the turbines. The region of momentum deficit gives rise to the IBL, above which the boundary layer is undisturbed by the dynamics near the surface, whereas inside the IBL, the flow structure changes downwind due to momentum extraction by the turbines. The growth of the IBL

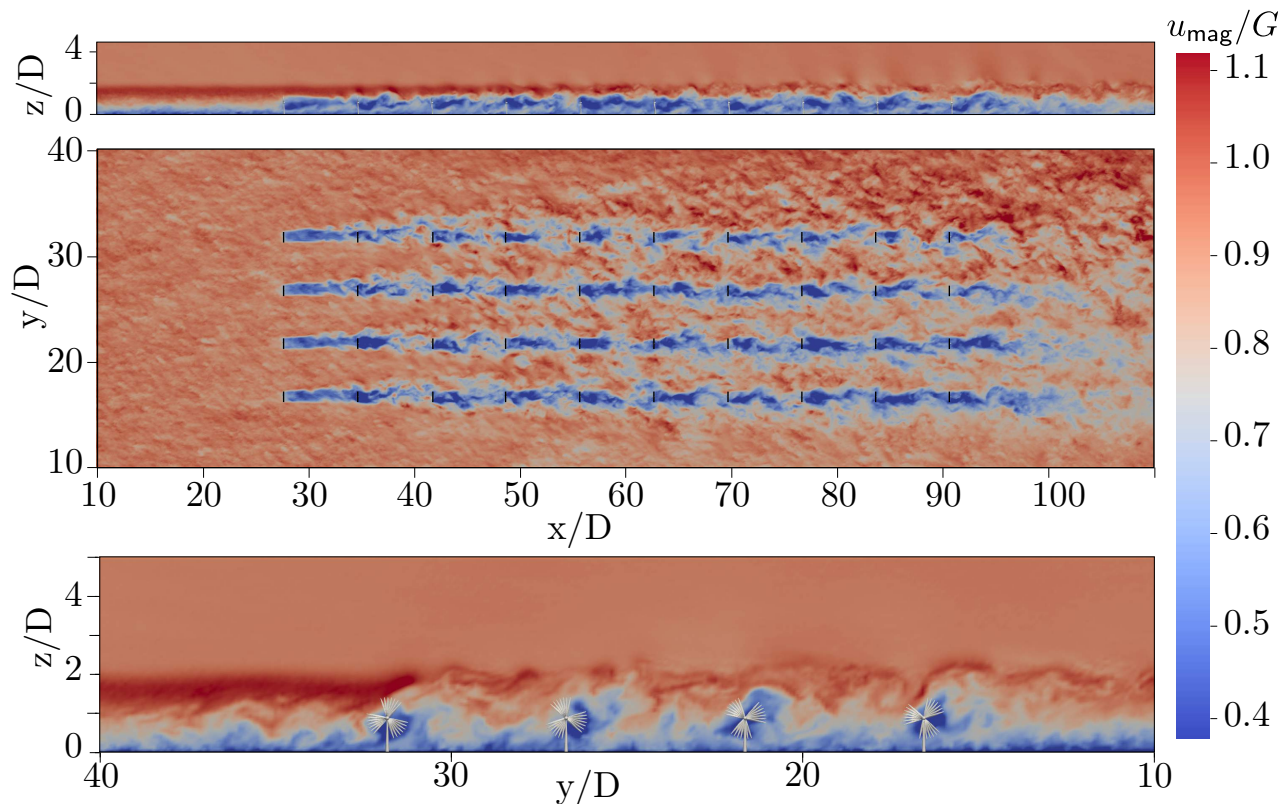


FIG. 4: Instantaneous velocity contours u_{mag}/G for the SBL-3 case. Top panel: Side view of the wind farm in an x - z plane through the middle of the 3rd turbine column from the bottom. Middle panel: Velocity contours at hub height (x - y plane). Bottom panel: Front view of the wind farm in an y - z plane passing through the fifth row.

shows how the wind farm modifies the flow. Furthermore, the height of the IBL is useful in analytical modeling of the wind farm power production [76]. There is no set rule for calculating the IBL height, for example, [47] define it as the height where the time-averaged wake velocity is 99% of the mean flow velocity at that height, Allaerts and Meyers (2017) [39] define it as the height where the ratio of time-averaged horizontal velocity magnitude and the inflow velocity at the same height, taken in a plane 2 km upwind, reaches a threshold of 97%, Stevens (2014) [77] defines it as the height where the vertical energy flux reaches the free stream value. We define the IBL as the height where the time-averaged horizontal velocity magnitude u_{mag} is 97% of the planar averaged inflow velocity at the same height. Besides, we fix the turbine top ($z_h + D/2$) as the minimum height of the IBL as the IBL grows over the turbine top. Figure 5(a) shows that the IBL height decreases when the surface cooling rate is increased and increases with the downstream location in the wind farm. The capping inversion height mostly determines the growth of the wind farm IBL. This is analogous to the growth of an IBL over a roughness change due to horizontal advection of air. Here, the wind farm is felt by the upstream flow as a roughness change, and due to the continuity constraint, the flow accelerates over the wind farm.

In a SBL the capping inversion gets pushed up by the growing IBL [39]. In figure 5(b), the base of the capping inversion z_c , defined as the height where the temperature gradient is maximum, is plotted along with the IBL for different cases. It is evident from the figure that the capping inversion is pushed up due to the IBL. For the first two cases, the IBL stays below the capping inversion. The displacement of the capping inversion increases with the increased cooling rate and for SBL-4, and SBL-5 the IBL grows above the capping inversion. The capping inversion is strongly stratified in these cases, and the Ri number of the flow is high at the top of the boundary layer. In these cases, the capping inversion acts as a lid, which limits the growth of the IBL. Due to the continuity constraint, the wind goes around the wind farm. The space between the top of the turbines and the capping inversion height determines how much wind flows around the wind farm. The capping inversion is at the height of $z_c/z_h \leq 2.114$ for cases SBL-3, SBL-4, SBL-5, which is approximately $0.5D$ or less above the tip of the turbines. In such a scenario, the fluid has very little room to go above the wind farm due to the stabilizing effect of the capping inversion. Consequently, in these cases, we see an appreciable amount of flow going around the wind farm. In essence, the so-called blockage due to the wind farm is the highest for SBL-5 and lowest for SBL-1, which is related to the space between the capping

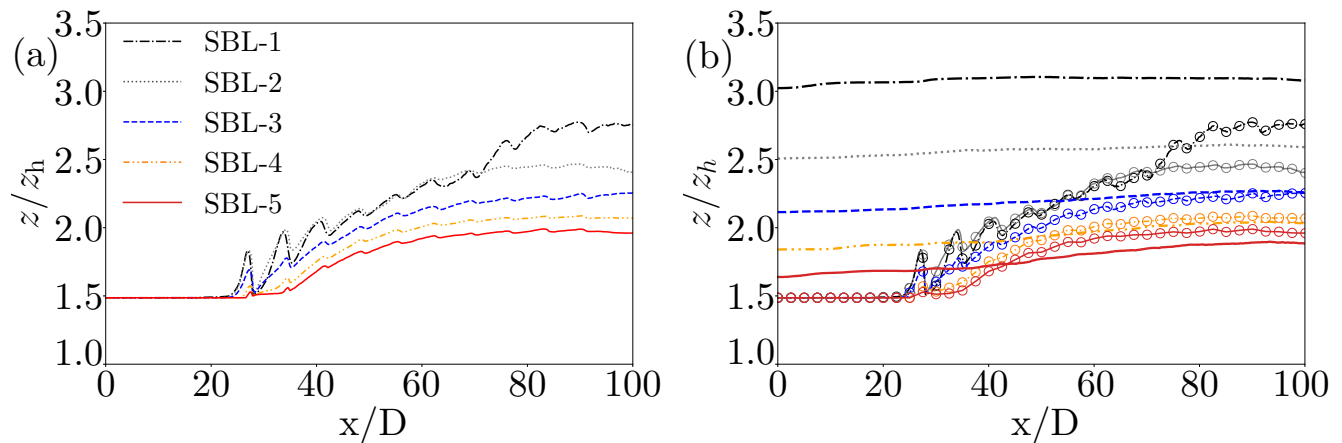


FIG. 5: (a) The development of the IBL height with streamwise distance. (b) The lines indicate the development of the the capping inversion height, and the lines with markers the IBL height as in panel (a). Note that for SBL-4, and SBL-5 the IBL grows above the capping inversion.

inversion and IBL.

Figures 6(a,b) show the time-averaged streamlines at hub height for the cases SBL-1 and SBL-5. Figure 6(a) shows the streamlines for SBL-1; we see that the streamlines are nearly parallel and show marginal divergence. Figure 6(b) shows the streamlines for the SBL-5 case; we observe significant streamline divergence proving that the flow goes around the wind farm. Rominger and Nepf (2011) [78] observe that when a flow encounters the leading edge of a canopy, a part of the flow is diverted, and the remaining part advects through the porous canopy. As the turbines start extracting energy, the shear in the IBL reduces, causing an increase in the Ri number in the IBL. The inset of figure 3(d) shows that the increase in Ri with height is maximum for SBL-5. As the shear in the flow decreases due to the energy extraction by the turbines the Ri increases. With the increase in local Ri, the flow stability increases, and the fluid finds it difficult to go over the wind farm, and it takes the path of least flow resistance, i.e., around the wind farm. The effect is similar to the flow going around a three-dimensional obstacle like a mountain under highly stratified conditions [79, 80].

Figures 6(c,d) show the pressure perturbation normalized by the inlet pressure at the base of the capping inversion z_c and at the hub height for the different cases. For SBL-5, the pressure perturbation starts increasing in the entrance of the wind farm when the IBL is at the same height as the capping inversion. As the capping inversion poses resistance to the developing IBL, the flow experiences an adverse pressure gradient. This makes it difficult for the flow to go through or above the wind farm, forcing it to go around.

IV. ENERGY BUDGET ANALYSIS

In the boundary layer, the wind turbines extract energy from the flow and entrain fresh momentum from the upper layers of the atmosphere. An energy budget analysis is a convenient way to understand the diverse phenomena involved in the power production of a wind farm. We follow the budget analysis by Allaerts and Meyers [39] on wind farms in conventionally neutral boundary layers. In section IV A, a budget analysis of the total energy and its different components is presented, and the turbine power production is discussed in section IV B.

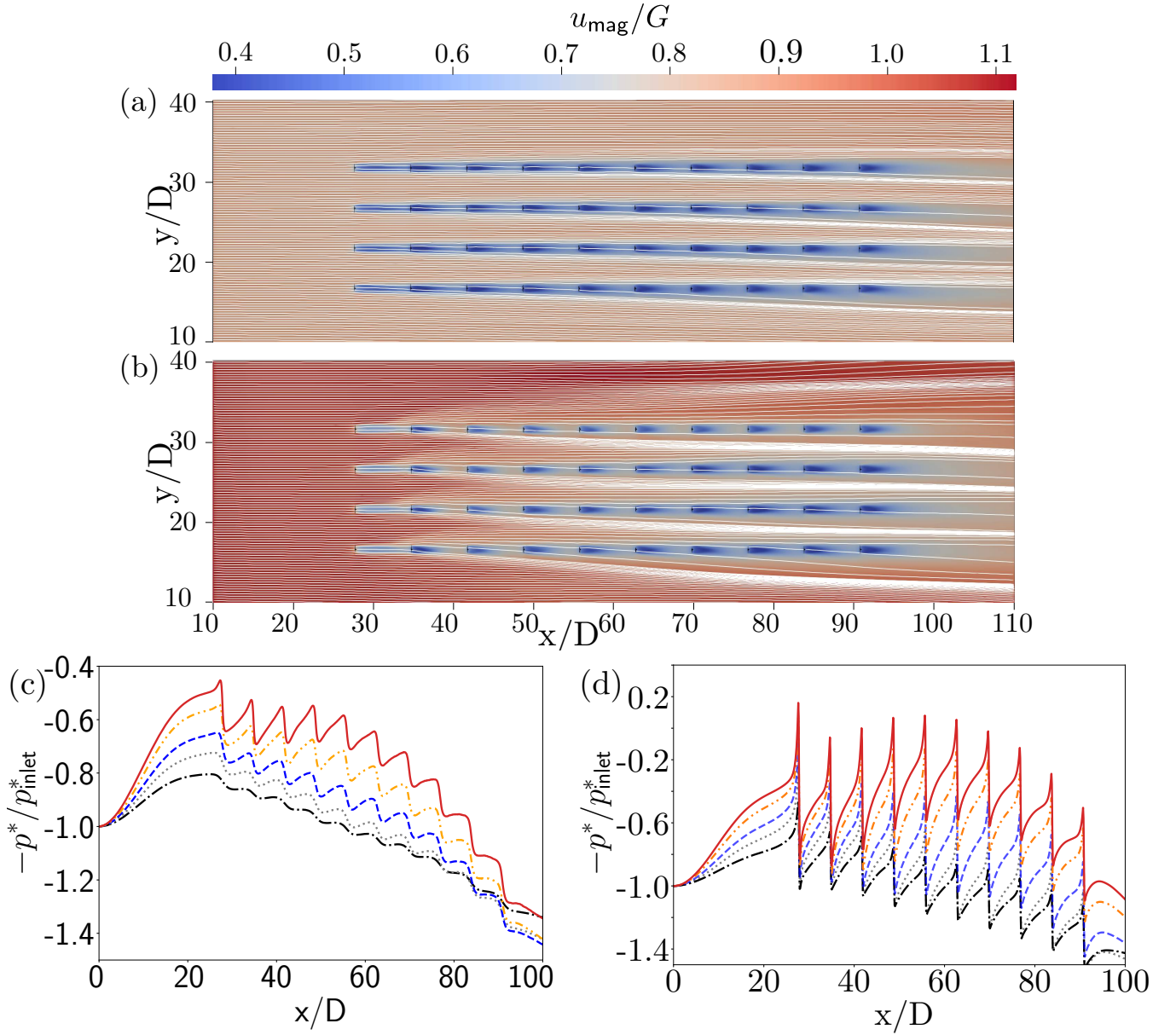


FIG. 6: Streamlines at the hub height for the (a) SBL-1 and (b) SBL-5 cases. Note that for SBL-5 in which the IBL pushes against the capping inversion, the streamlines indicate that there is very significant flow around the farm. (c) Pressure perturbation at the capping inversion as function of streamwise distance. The pressure perturbation at the capping inversion increases with increasing cooling rate. The flow experiences maximum adverse pressure gradient for SBL-5. (d) The variation of pressure perturbation at hub height with the streamwise distance. In (c) and (d) p_{inlet}^* is the pressure perturbation at the inlet.

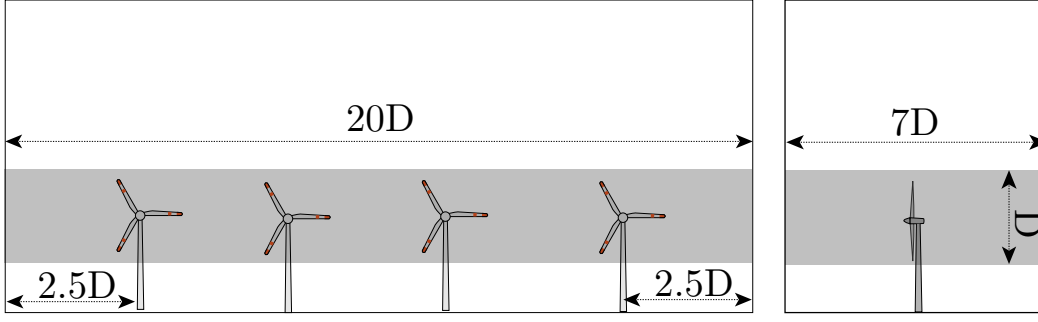


FIG. 7: Shaded area represents the control volume used in the budget analysis. The control volume for each column has a dimension of $7D \times 20D \times D$, and starts at a height of $z_h - D/2$.

A. Entrainment, streamwise flow work

The steady-state, filtered energy equation is obtained by operating the momentum equation with \tilde{u}_i and performing time averaging [39, 81]. The energy equation is,

$$\begin{aligned}
 & \underbrace{\overline{u_j \partial_j \left(\frac{1}{2} \overline{u_i u_i} + \frac{1}{2} \overline{u'_i u'_i} \right)}}_{\text{Kinetic energy flux}} + \underbrace{\partial_j \left(\frac{1}{2} \overline{u'_j u'_i u'_i} + \overline{u_i u'_i u'_j} \right)}_{\text{Turbulent transport}} + \underbrace{\overline{\partial_j (u_i \tau_{ij})}}_{\text{SGS transport}} = \underbrace{-\overline{\partial_i (p u_i)}}_{\text{Flow work}} \\
 & + \underbrace{g\beta(\overline{u_i \theta} - \overline{u_i \theta_0}) \delta_{i3}}_{\text{Buoyancy}} + \underbrace{f_c(\overline{u_i U_g}) \delta_{i2} - f_c(\overline{u_i V_g}) \delta_{i1}}_{\text{Geostrophic forcing}} + \underbrace{\overline{f_i u_i}}_{\text{Turbine power}} + \underbrace{\overline{\tau_{ij} S_{ij}}}_{\text{Dissipation}},
 \end{aligned} \tag{9}$$

where, the overline represents time averaging, and $\overline{u'_i u'_j} = (\overline{u_i u_j} + \overline{\tau_{ij}}) - \overline{u_i} \overline{u_j}$ represents the momentum flux to which the SGS components have been added. We are interested in the total power production per wind turbine row and energy balance around each turbine. To calculate the total energy, we numerically integrate the terms in (9) in a control volume \forall surrounding each turbine row. Figure 7 schematically represents the dimensions and the extent of the aforementioned control volume. The control volume covers all the turbines in a row and has a streamwise extent of $s_x D$, i.e. $7D$, with $3.5D$ in front and $3.5D$ behind the turbines, in the streamwise direction [39]. In the vertical direction, the control volume has a dimension of D , and covers the volume between $z_h - D/2$ and $z_h + D/2$. In the spanwise direction the control volume covers the whole row with an additional $2.5D$ on the sides, essentially $20D$. So the total control volume size for each row is, $7D \times 20D \times D$. Integrating (9) and rearranging gives

$$\begin{aligned}
 \underbrace{\int_{\forall} \overline{f_i u_i} d\forall}_{\mathbb{P}, \text{ Turbine power}} &= \underbrace{\int_S \overline{u_j} \left(\frac{1}{2} \overline{u_i u_i} + \frac{1}{2} \overline{u'_i u'_i} \right) dS_i}_{\mathbb{E}_k, \text{ Kinetic energy flux}} + \underbrace{\int_S \left(\frac{1}{2} \overline{u'_j u'_i u'_i} + \overline{u_i u'_i u'_j} \right) dS_i}_{\mathbb{T}_t, \text{ Turbulent transport}} + \underbrace{\int_S \overline{(u_i \tau_{ij})} dS_i}_{\mathbb{T}_{\text{sgs}}, \text{ SGS transport}} + \underbrace{\int_S \overline{(p u_i)} dS_i}_{\mathbb{F}, \text{ Flow work}} \\
 &- \underbrace{\int_{\forall} g\beta(\overline{u_i \theta} - \overline{u_i \theta_0}) \delta_{i3} d\forall}_{\mathbb{B}, \text{ Buoyancy}} - \underbrace{\int_{\forall} f_c(\overline{u_i U_g}) \delta_{i2} - f_c(\overline{u_i V_g}) \delta_{i1} d\forall}_{\mathbb{G}, \text{ Geostrophic forcing}} - \underbrace{\int_{\forall} \overline{\tau_{ij} S_{ij}} d\forall}_{\mathbb{D}, \text{ Dissipation}}.
 \end{aligned} \tag{10}$$

In equation 10, \mathbb{E}_k represents the divergence of the kinetic energy flux, which includes both the resolved and the SGS kinetic energy, the turbulent transport term \mathbb{T}_t , which includes the entrainment of mean momentum due to turbulence and the entrainment of turbulent kinetic energy due to fluctuating velocities (third order terms), \mathbb{T}_{sgs} represents the transport of momentum due to SGS fluxes. The flow work \mathbb{F} represents the energy transfer due to static pressure drop of the flow across a turbine. The term \mathbb{B} represents the turbulence destruction due to buoyancy, \mathbb{G} represents the mean geostrophic forcing, and finally \mathbb{P} represents the turbine power production.

We are interested in the contribution of different budget components to power production. Therefore all the terms are normalized by the magnitude of the power produced by the first turbine row. The SGS transport \mathbb{T}_{sgs} and the buoyancy fluxes \mathbb{B} are small, less than 10% of the first-column power and have been left out of the plots for brevity. The terms in equation (10), which include the gradients i.e. \mathbb{E}_k , \mathbb{T}_t , \mathbb{T}_{sgs} , and \mathbb{F} , represent the net flux out of the control volume, for example, $\mathbb{E}_k = \mathbb{E}_{\text{out}} - \mathbb{E}_{\text{in}}$. Positive values of these terms $\mathbb{E}_{\text{in}} > \mathbb{E}_{\text{out}}$ indicate that more energy is added to the control volume than removed. This indicates that in the control volume energy is extracted from the

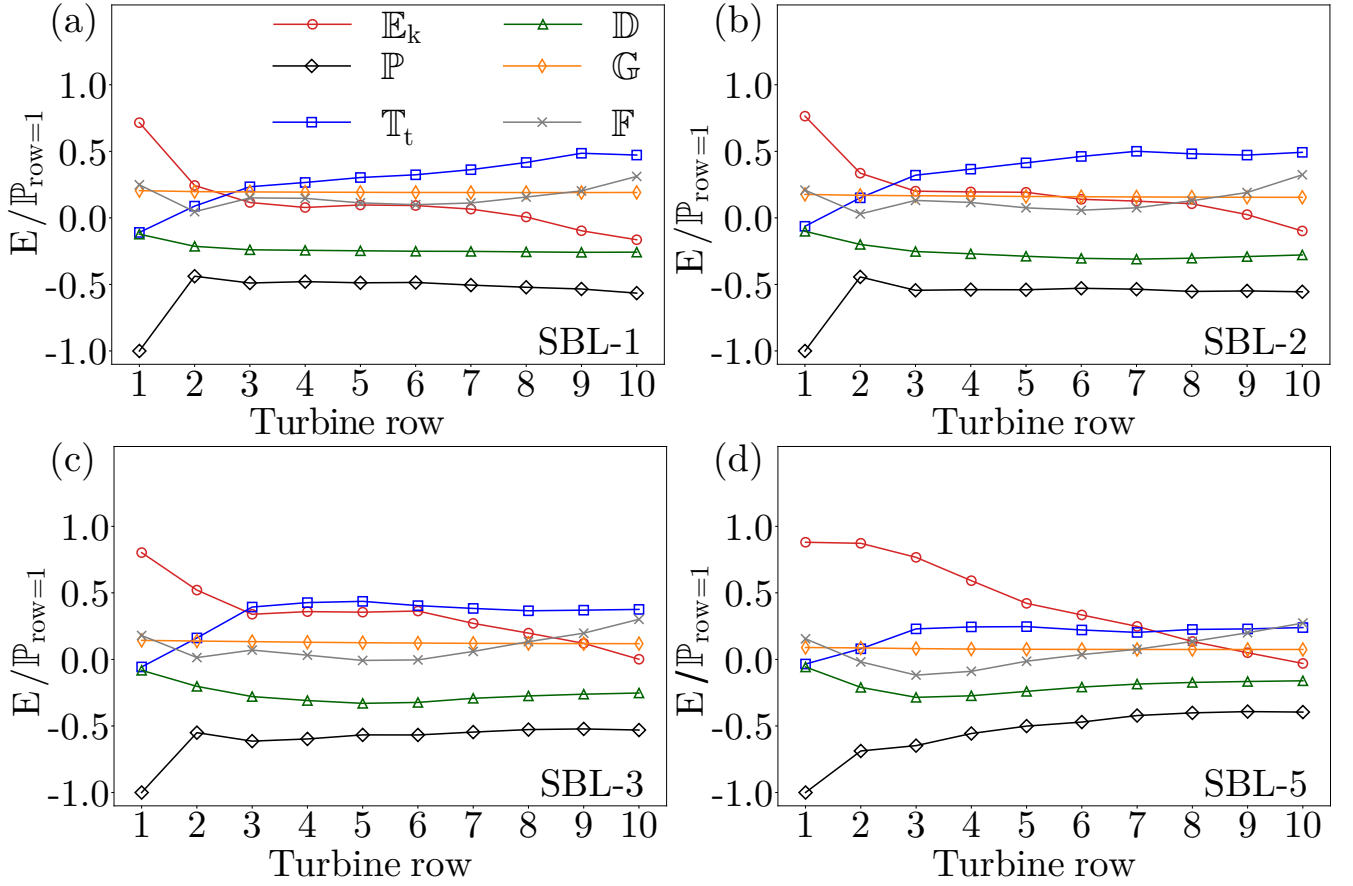


FIG. 8: Energy budget for cases (a) SBL-1, (b) SBL-2, (c) SBL-3, and (d) SBL-5. All the terms are normalized by the power production of the first turbine row. The symbols in the legend are defined in equation (10) and information about the cases can be found in table I.

flow by the turbines or other means. Negative values of these terms indicate $\mathbb{E}_{\text{out}} > \mathbb{E}_{\text{in}}$, which means energy is being added to the flow.

For all the cases, the geostrophic forcing term \mathbb{G} remains nearly constant for all the rows of the wind farm, representing a constant driving force. Besides \mathbb{G} , there are three primary energy sources, which determine the turbine power production, namely (i) the kinetic energy flux \mathbb{E}_k , (ii) the work done due to the static pressure drop \mathbb{F} , and (iii) the turbulent transport \mathbb{T}_t , which includes both entrainment of mean momentum into the wind farm by turbulent fluxes (shear production term) and the entrainment due to turbulent fluxes (third-order turbulence terms). Major energy sinks are the power extracted by the turbines \mathbb{P} , the dissipation \mathbb{D} , and the turbulence destruction due to buoyancy \mathbb{B} .

Figure 8(a) shows different energy components for the SBL-1 case. The turbines continuously extract energy from the flow, and the kinetic energy flux decreases in the downstream direction. For the last three rows, $\mathbb{E}_k < 0$, which means more energy exits the control volume than entering it. This happens because of the entrainment of the kinetic energy \mathbb{T}_t from fluid above the wind farm. The turbulent transport term \mathbb{T}_t is composed of fluxes like $\bar{u} \cdot \overline{u'w'}$ and $\bar{v} \cdot \overline{v'w'}$, which represent the vertical (downward) flux of the mean momentum created by turbulence, i.e. entrainment of mean energy from above towards the turbines. With more and more turbulence created by the turbine wakes, this entrainment flux increases in the downstream direction. In a wind farm operating under neutral stratification and no capping inversion or LLJ, this entrainment flux is of the same order of magnitude as the turbine power production. This flux acts as the major source of power for the downstream wind turbines and reaches a constant value towards the end of the wind farm [23, 24]. A similar variation of energy fluxes has been reported by in the simulations of wind farms in conventionally neutral boundary layers [39]. For SBL-1, the jet height ($z_{\text{jet}}/z_h = 2.670$) is well above the wind farm. The IBL grows above the wind farm and facilitates the interaction with the high-velocity jet. Consequently, the entrainment continuously increases downstream and reaches its maximum towards the end of the wind farm. Figure 9 shows that although the jet strength reduces for SBL-1, the jet more or less persists above the entire wind farm.

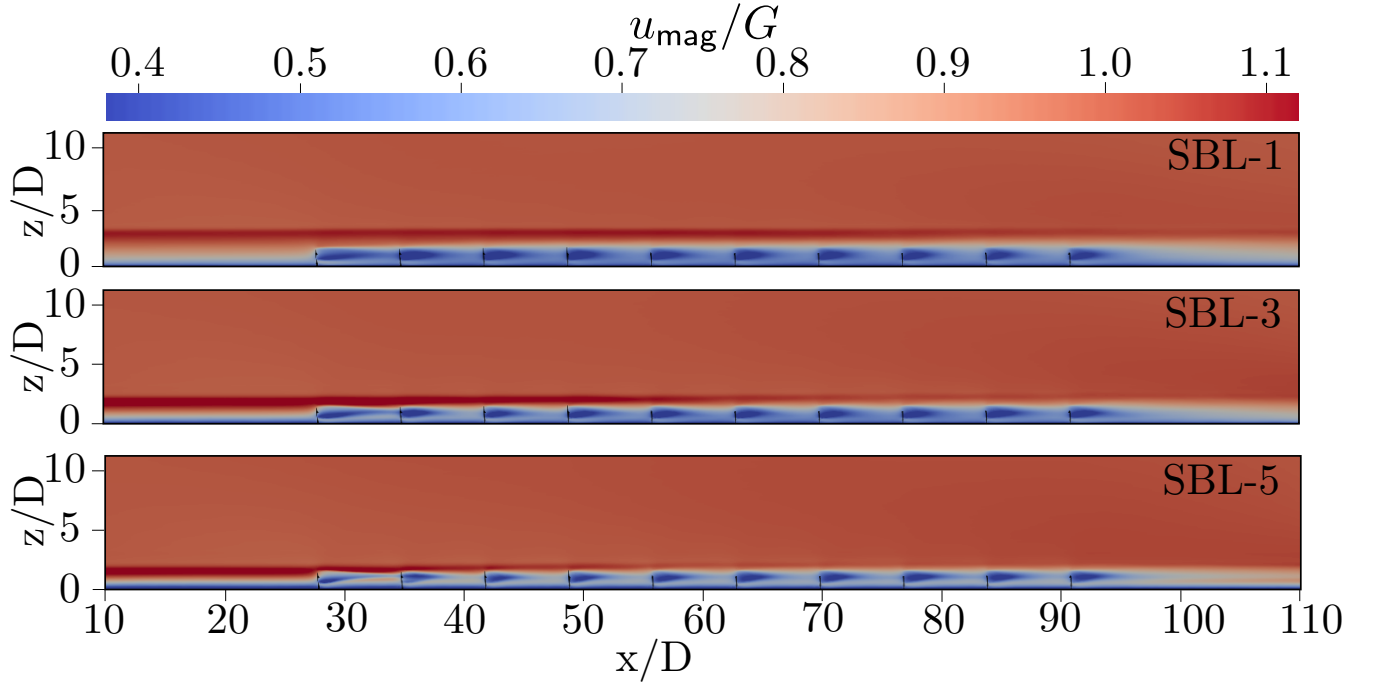


FIG. 9: Streamwise velocity contour for different cases. Note that the strength of the LLJ is negligible towards the rear for the wind farm for SBL-5.

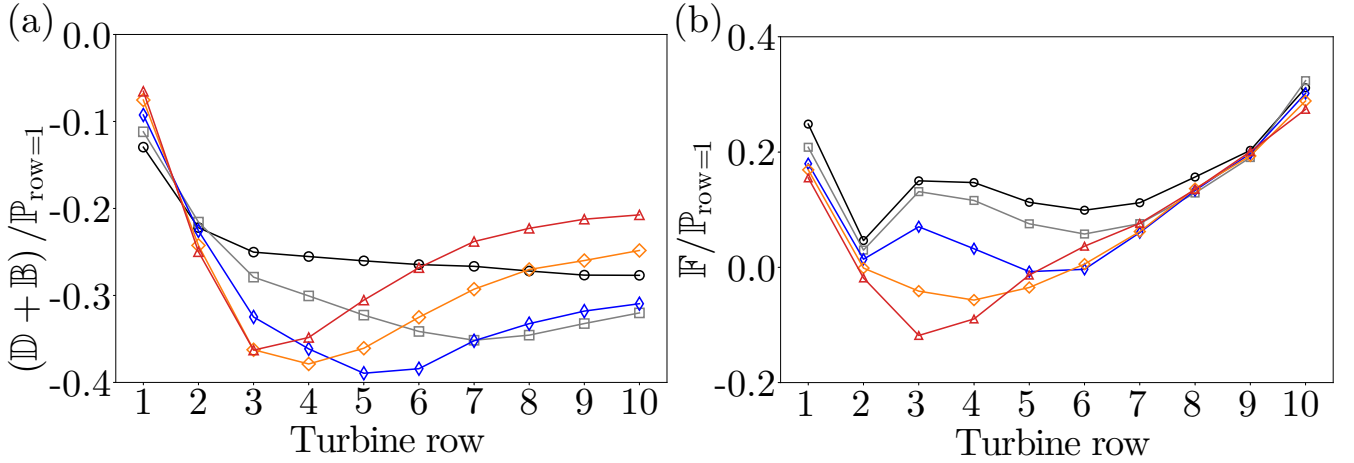


FIG. 10: (a) Turbulence destruction due to buoyancy and dissipation, $\mathbb{B} + \mathbb{D}$ (b) Flow work \mathbb{F} represents the work done due to pressure drop.

Figure 8(a) shows that the pressure-velocity correlation due to the static pressure drop, also known as the flow work \mathbb{F} , is positive and increases along the length of the wind farm. This is an indication that the turbines operate in a favorable pressure gradient in the SBL-1 case. \mathbb{F} has a significant contribution towards the power production near the end of the wind farm. The turbine power production, which is the major sink, is maximum at the entrance and reduces downwind due to the effect of the upstream turbine wakes. This variation is typical for a wind farm with an aligned layout and has been observed both in observations and numerical studies [47, 68, 82]. The dissipation \mathbb{D} acts as an additional energy sink and remains roughly constant as a function of the downstream position in the wind farm.

Figure 8(b) presents the energy budget for the SBL-2 case. The figure shows that the entrainment \mathbb{T}_t increases until the 7th row when it saturates. A similar trend is observed for the SBL-3 case in figure 8(c), but then the entrainment already saturates after the 5th row. For SBL-3 the jet height ($z_{\text{jet}}/z_h = 1.836$) is slightly above the turbine tip height. The increase and decrease in entrainment correspond to the positions when the wind farm IBL starts interacting with the LLJ. Figure 9 shows that the jet strength for SBL-3 is significantly reduced after the 5th row. For SBL-5, the jet

is utilized by a couple of rows at the entrance, and the remaining rows have little or no jet left to entrain, therefore \mathbb{T}_t remains nearly constant for this case after the initial increase.

Figure 10(a) shows the variation of $\mathbb{D} + \mathbb{B}$ for different cases. Both \mathbb{B} and \mathbb{D} act as energy sinks in the budget and the buoyancy flux \mathbb{B} is small, less than 8% of the first-row power for all the cases, therefore \mathbb{B} is combined with \mathbb{D} to represent the net energy sink. $\mathbb{B} + \mathbb{D}$ is maximum when the turbines interact with the LLJ. This shows that the turbulence production due to mean shear is maximum when the LLJ is at lower heights. In SBL-5, for which the stability is the highest (see figure 8(d)), \mathbb{T}_t is nearly equal to \mathbb{D} , which means there is no effect of entrainment fluxes on the turbine power production and we see a continuous drop in the kinetic energy flux as well as power production. Under stable stratification, increasing the stability damps out the vertical velocity fluctuations, which results in a reduction of in the downward transport of horizontal momentum towards the surface (see figure 3(d)). This results in a reduction of shear production terms $\overline{u'w'}\partial\overline{u}/\partial z$ and $\overline{v'w'}\partial\overline{v}/\partial z$ in \mathbb{T}_t , which causes a reduction of the turbulent kinetic energy. As mentioned before, the absolute value of \mathbb{B} is not significant. However, the turbulent fluctuations damped out by the stratification, in turn, affect the momentum flux, which causes the weak turbulence in the SBL [83]. With the jet utilized by the first few turbine rows in SBL-5, the turbines downstream experience a reduction in shear production as well as mean shear. Consequently, we see a continuous decrease in power production for the turbines further downstream.

Monin and Yaglom (1971) [84] describe the Obukhov length as the height below which buoyancy or the thermal effects do not play an important role. In a SBL, for $z \ll |L|$, the effects of dynamic factors such as shear dominate. For $z > |L|$ the thermal effects dominate diminishing turbulence. The Obukhov length for cases SBL-5 and SBL-4 are 48.8 m and 66.0 m, respectively, which is less than the turbine hub height. In these cases, the turbines operate mostly in a buoyancy dominated region with high stability. Therefore, we see minimal shear production and turbulent transport \mathbb{T}_t in these cases. Here, \mathbb{T}_t is more or less balanced by $\mathbb{B} + \mathbb{D}$ (figure 8(d)) and the turbine power production depends completely on non-turbulent phenomena such as the divergence of mean kinetic energy flux and the static pressure drop. With the increased shear associated with LLJ, the turbines in a SBL produce more power compared to the turbines operating in the absence of a LLJ. For cases with high stability i.e. $z_h < |L|$, \mathbb{E}_k , \mathbb{F} , and \mathbb{G} are the only energy sources available, as \mathbb{T}_t is balanced by $\mathbb{B} + \mathbb{D}$. Therefore, the power production decreases with increasing stratification. However, even in such cases, in the presence of a LLJ, the front turbine rows may still perform well due to the elevated shear in the LLJ.

Figure 10(b) presents the variation of the flow work \mathbb{F} for different cases. SBL-1, SBL-2, and SBL-3 show that the flow work is always positive, which shows that the turbines operate under a favorable pressure gradient. Since $\mathbb{F} > 0$, it acts as an energy source for the turbine power production for the cases SBL-1, SBL-2, and SBL-3. For the case SBL-5, with the increase in streamwise distance, the resistance to the flow created by the capping inversion increases as the IBL grows. This resistance to the flow reaches a maximum at the third turbine column (approximately $x/D \approx 45$) when the IBL height is the same as the height of capping inversion, and we see the minimum of \mathbb{F} at this point. Following this critical point, the flow starts going around the wind farm, facilitating the easier flow, and the consequent pressure drop across the wind farm increases.

B. Turbine power production

Figure 11(a) presents the row-averaged power normalized by the average power production of the turbines in the first row of SBL-1. The figure shows that the power production of the first turbine row increases significantly when the surface cooling is increased. The reason is that the average hub height velocity is higher for the cases with stronger stratification, see figure 3(a). However, the figure shows that the turbine power production towards the end of the wind farm is lower for cases SBL-4 and SBL-5 than for SBL-3. The reason is that the turbulent energy entrainment further downstream in the wind farm is limited for these cases. To study the effect of wake recovery on the performance of downstream turbine rows for the different cases, figure 11(b) presents the row-averaged power normalized by the power production of the first row. An increase in power production after the second row indicates high turbulence activity and faster relative wake recovery, and a continuous decrease in power indicates slower wake recovery. For SBL-1 the $\mathbb{P}/\mathbb{P}_{\text{row}=1}$ increases downstream of the first turbine. This increase in the relative power production with the downstream direction indicates that more energy is entrained from the jet which is then extracted by the turbines. For SBL-4 and SBL-5 $\mathbb{P}/\mathbb{P}_{\text{row}=1}$ decreases asymptotically to a constant value indicating reduced relative wake recovery.

Figure 12(a) and (b) show the turbulent entrainment and wake recovery for different cases. In the region behind the fifth row, the SBL-3 case shows maximum entrainment. For this case, the jet height is $z_{\text{jet}}/z_h = 1.836$ and the vertical meandering of the turbine wakes can entrain the high velocity jet, this interaction reaches a maximum around the 3rd turbine row after which the jet is completely used up and the entrainment continuously decreases. Figure 12(b) shows that SBL-1 has the fastest wake recovery of all the cases. The inlet turbulence intensity at the hub height

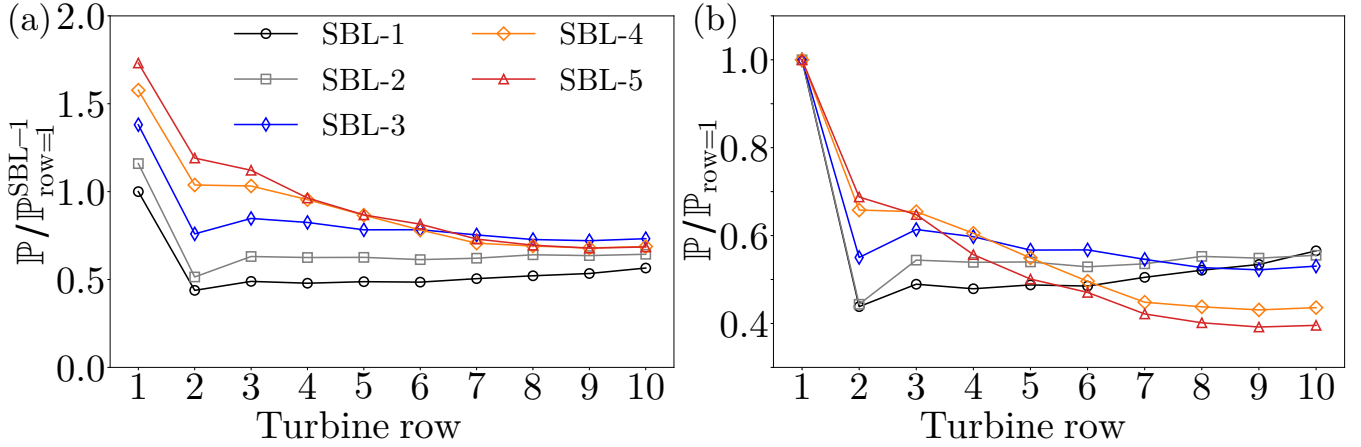


FIG. 11: (a) Power production normalized with the first row average power of SBL-1. (b) Power production normalized with the first row power.

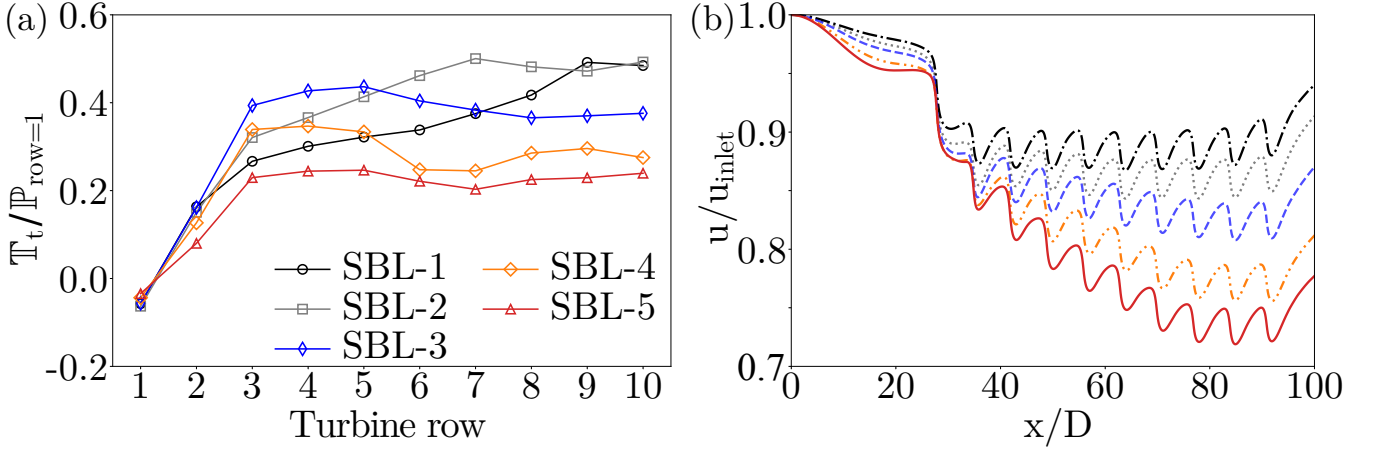


FIG. 12: (a) The development of the turbulent transport term T_t , see equation (10), as function of the downstream position for different cases, see table I. (b) Plot of streamwise velocity development at the hub height normalized by the inlet velocity for different cases.

for this case is the highest with $TI_{z_h} = 5.82\%$. Cases SBL-2 and SBL-3 show significant wake recovery towards the end of the wind farm. For these cases the inlet Obukhov length is 189 and 100 meters, respectively, which is greater than the hub height. This means that the turbines are in a regime where the shear generated turbulence effects dominate. As a result of the turbulence generated towards the end of the wind farm, these cases show significant wake recovery. Figure 12(b) shows a significant reduction in the upstream wind velocity in front of the first turbine row, which indicates the effect of the adverse pressure gradient created by the wind farm blockage. This upstream reduction in wind speed increases with stratification and is highest for SBL-5 for which the adverse pressure gradient caused by the capping inversion is maximum. This flow blockage reduces the inlet wind velocity for the first row of turbines, and the turbines produce lesser power than what they would if they were free-standing. Similar upwind flow reduction has been observed in previous studies of wind farm flow blockage [40, 85–87].

V. EFFECT OF WIND VEER

In the presence of the Coriolis force, the wind follows an Ekman spiral in which the wind velocity vector changes its direction with height. The changes in the wind angle are caused by the imbalance between the pressure gradient and frictional forces. Under stable stratification, the Ekman spiral is very pronounced, and it produces a wind veer facilitated by the significant spanwise flow. In our simulations, we use a PI controller to fix the wind angle at the hub height to zero [57]. This results in a flow that has a positive spanwise velocity below the turbine hub and a negative spanwise velocity above the turbine hub. The flow is turned such that the natural wind veer leads to these velocities

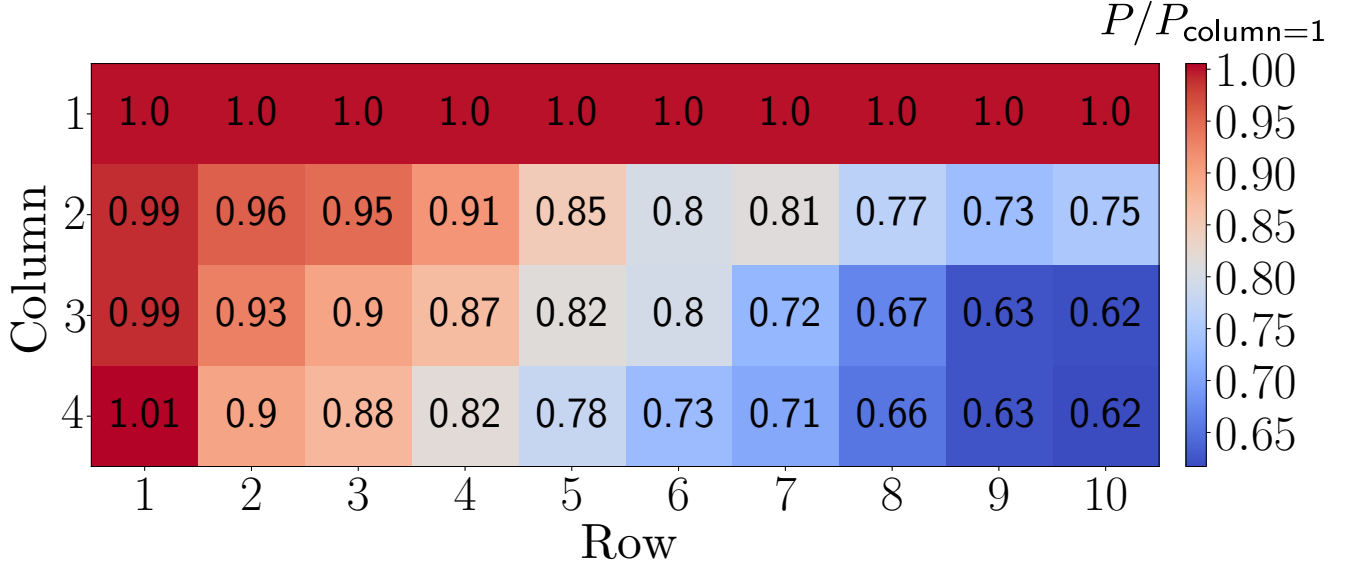


FIG. 13: Power map for the case SBL-3. All the entries have been normalized by the power of the first column. Due to the wind veer, the first column produces more power compared to the other columns.

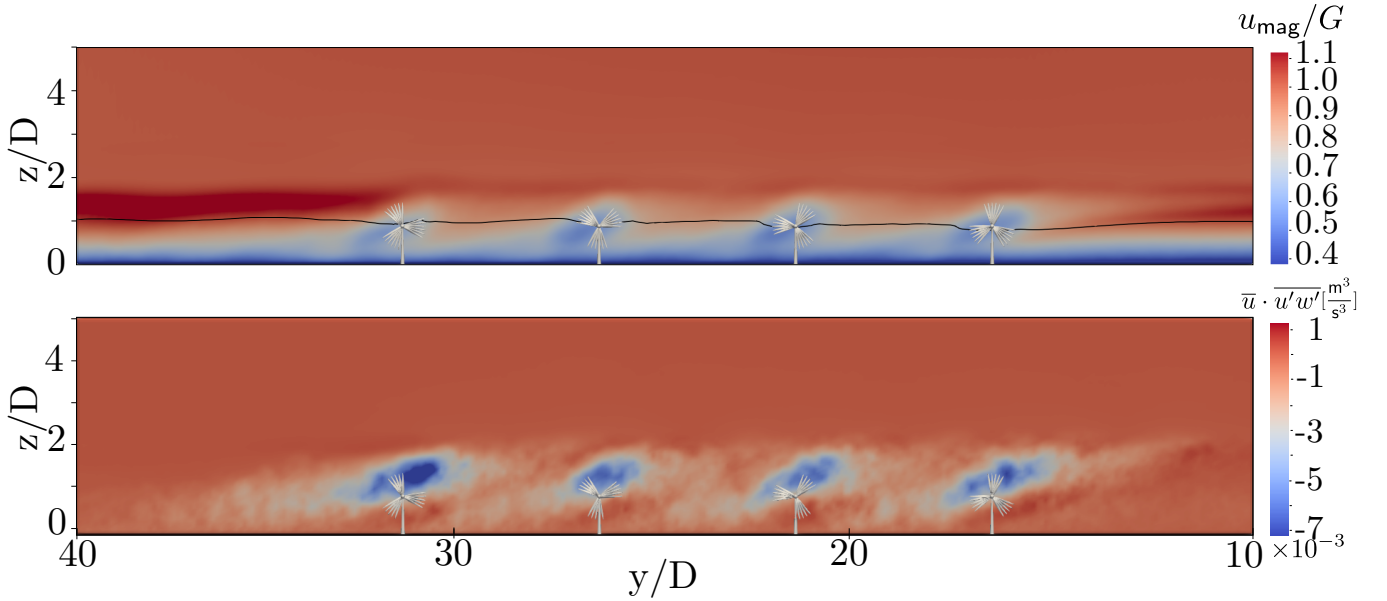


FIG. 14: The (a) normalized horizontal velocity magnitude u_{mag}/G and (b) the energy flux $\bar{u} \cdot \overline{u'w'}$ in the y - z plane, passing through the 6th turbine row. The black line represents the surface with zero spanwise velocity ($v = 0$). Above the line, the flow goes to the right, and below the line, the flow is going to the left.

in the frame of reference that we pick.

Figure 13 presents the power map for the SBL-3 case with all the entries normalized by the power produced by the turbines in the 1st column of their respective rows. It is evident from the figure that the turbines in the 1st column produce more power compared to the rest of the turbine columns. Furthermore, there is a gradual reduction in power production towards the fourth column. This variation in power is because of the wind veer created by the Coriolis force. We find that this effect is substantial for SBL-3, SBL-4, and SBL-5. The effect is certainly present for SBL-1 and SBL-2 but not significant.

Figure 14(a) shows the horizontal velocity magnitude for the SBL-3 case in the y - z plane cut through the middle of the 6th turbine row. In this case, the jet height is $z_{jet}/z_h = 1.836$, which is slightly above the turbines. We observe

that the turbines completely utilize the jet above the wind farm due to entrainment and wake meandering, whereas the jet to the left of the 1st turbine column provides a continuous supply of fresh momentum due to the spanwise flow which goes to the right. The turbines on the left in figure 14 get a constant supply of high-speed jet, which is utilized by the turbines, and the remaining fluid goes to the turbines on the right. As the 1st column has already utilized the jet, the power production of the next column is reduced. Furthermore, the local variation in the wind velocity created by the turbine wakes also causes the wind to deflect clockwise. The deflection of the turbine wakes clockwise in the Northern hemisphere is due to the imbalance created by the entrainment fluxes induced by the wind farm [43, 57]. We observe a similar clockwise deflection of the turbine wakes as a result of which the turbines in the inner columns operate in the wake of the outer columns.

Figure 14(b) shows the streamwise downward energy flux $\bar{u} \cdot \overline{w'w'}$ for the SBL-3 case. The wake structure is skewed due to the lateral shear created by the spanwise flow. The turbine in the 1st column entrains most energy from the jet, and the subsequent columns entrain less energy from the jet due to the wind turbine wake. This skewed spatial structure of energy entrainment is an additional reason for the observed power variation.

VI. CONCLUSIONS

Large-eddy simulations of wind farms in stable boundary layers were carried out in the present study. The objective of the study was two-fold: 1) to study the variation of wind farm power production with the LLJ height and 2) to study the effect of stable stratification and low-lying capping inversion on the flow development in wind farms. The study was carried out by systematically varying the cooling rate at the surface, which gives rise to boundary layers with capping inversions and LLJs at various heights.

Decreasing the cooling rate reduces the turbulence near the surface, which in turn increases the geostrophic components in the boundary layer producing LLJs with increased strength. With increasing stratification, the height of the capping inversion reduces, offering increased resistance to the flow. Due to the adverse pressure gradient created by the capping inversion and the blockage created by the presence of a wind farm, the flow goes around the wind farm. When the capping inversion is significantly above the IBL height, the flow accelerates over the wind farm. However, when the IBL height and the capping inversion height are similar, flow goes around the wind farm. Therefore, performing simulations with periodic boundary conditions in the spanwise direction over-predicts the flow blockage as the flow cannot go around the wind farm. LES of conventionally neutral wind farms [39, 87] show such flow blockage for ‘infinite’ wind farms.

The presence of a LLJ can be beneficial to wind farm power production depending on the LLJ height. When the jet is above the wind farm, it serves as a source of high momentum for the turbines to entrain. We observe increased entrainment when the jet is above the wind farm. The entrainment is maximum when the turbine wakes can directly interact with the jet by the vertical meandering of the turbine wakes. The entrainment reduces once the turbines entrain all the energy in the jet. If the LLJs are at a height $z_{\text{jet}} \leq z_h + D/2$, the turbines at the entrance which can directly interact with the LLJ perform significantly better than the inner turbines. Under similar stability conditions, i.e., stable stratification, a wind farm performs better if the LLJ is present above the wind farm than when a LLJ is absent. The simulations show that the turbine rows at the entrance utilize the LLJ and the entrainment decreases after the jet is completely exhausted. Therefore, wind farms with higher aspect ratios (spanwise width-to-streamwise length ratio of the wind farm) are more beneficial than long wind farms with low aspect ratios, at sites where LLJs are prominent.

Stable atmospheric boundary layers generally have low turbulence intensities, and the surface Obukhov length can serve as an important length scale to predict the impact of the stability. We find that for $z_h \gg |L|$ the shear effects dominate, and the entrainment is more than the dissipation and buoyancy destruction. When $z_h < |L|$ the thermal effects dominate, and there is very little entrainment as buoyancy damps out the vertical velocity fluctuations reducing both vertical kinetic energy and downward turbulent fluxes.

In the presence of a LLJ, an appreciable spanwise flow is created by the wind veer. Consequently, the turbines which can directly interact with the LLJ (e.g. turbines in the left column in figure 14) produce more power than the rest of the turbines. The rest of the turbines can only interact with the LLJ via turbulent entrainment. This effect is prominent only if the jet height $z_{\text{jet}} \approx z_h + D$. Finally, the present study only focuses on the cases where the jet is above the turbine top height, i.e. $z_{\text{jet}} \geq z_h + D/2$, consequently the turbines only experience positive shear in the LLJ. Further studies are required to analyze the effect of negative shear of the LLJ (when $z_{\text{jet}} < z_h + D/2$) on the wind farm power production.

Acknowledgements: This work is part of the Shell-NWO/FOM-initiative Computational sciences for energy research of Shell and Chemical Sciences, Earth and Live Sciences, Physical Sciences, FOM, and STW. This work was carried out on the national e-infrastructure of SURFsara, a subsidiary of SURF corporation, the collaborative ICT organization for Dutch education and research.

References

-
- [1] A. Smedman, U. Högström, and H. Bergström, Low level jets—a decisive factor for off-shore wind energy siting in the baltic sea, *Wind Engineering*, 137 (1996).
- [2] A. K. Blackadar, Boundary layer wind maxima and their significance for the growth of nocturnal inversions, *Bull. Amer. Meteor. Soc.* **38**, 283 (1957).
- [3] A. J. Thorpe and T. H. Gymer, The nocturnal jet, *Q. J. R. Meteorol. Soc.* **103**, 633 (1977).
- [4] L. Mahrt, Stratified atmospheric boundary layers, *Boundary-Layer Meteorol.* **90**, 375 (1999).
- [5] L. Mahrt, Nocturnal boundary-layer regimes, *Boundary-Layer Meteorol.* **88**, 255 (1998).
- [6] P. Baas, F. C. Bosveld, H. K. Baltink, and A. A. M. Holtslag, A climatology of nocturnal low-level jets at Cabauw, *J. Appl. Meteor. Climatol.* **48**, 1627 (2009).
- [7] R. M. Banta, Stable-boundary-layer regimes from the perspective of the low-level jet, *Acta Geophysica* **56**, 58 (2008).
- [8] T. V. Prabha, B. N. Goswami, B. S. Murthy, and J. R. Kulkarni, Nocturnal low-level jet and atmospheric streams over the rain shadow region of indian western ghats, *Q. J. R. Meteorol. Soc.* **137**, 1273 (2011).
- [9] N. Kelley, M. Shirazi, D. Jager, S. Wilde, J. Adams, M. Buhl, P. Sullivan, and E. Patton, Lamar low-level jet project interim report, National Renewable Energy Laboratory, National Wind Technology Center, Golden, CO, Technical Paper No. NREL/TP-500-34593 (2004).
- [10] R. M. Banta, R. K. Newsom, J. K. Lundquist, Y. L. Pichugina, R. L. Coulter, and L. Mahrt, Nocturnal low-level jet characteristics over Kansas during CASES-99, *Boundary-Layer Meteorol.* **105**, 221 (2002).
- [11] J. K. Lundquist, Intermittent and elliptical inertial oscillations in the atmospheric boundary layer, *J. Atmos. Sci.* **60**, 2661 (2003).
- [12] P. C. Kalverla, J. B. D. Jr., G.-J. Steeneveld, and A. A. M. Holtslag, Low-level jets over the North Sea based on ERA5 and observations: together they do better, *Wind Energy Science* **4**, 193 (2019).
- [13] A.-S. Smedman, M. Tjernström, and U. Högström, Analysis of the turbulence structure of a marine low-level jet, *Boundary-Layer Meteorol.* **66**, 105 (1993).
- [14] K.-P. Wittich, J. Hartmann, and R. Roth, On nocturnal wind shear with a view to engineering applications, *Boundary-Layer Meteorol.* **37**, 215 (1986).
- [15] F. Beyrich, Sodar observations of the stable boundary layer height in relation to the nocturnal low-level jet, *Meteorologische Zeitschrift. Neue Folge (Berlin)* **3**, 29 (1994).
- [16] F. Liechti and E. Schaller, The use of low-level jets by migrating birds, *Naturwissenschaften* **86**, 549 (1999).
- [17] D. L. Sisterson and P. Frenzen, Nocturnal boundary-layer wind maxima and the problem of wind power assessment., *Environ. Sci. Technol.* **12**, 218 (1978).
- [18] W. Gutierrez, A. Ruiz-Columbie, M. Tutkun, and L. Castillo, Impacts of the low-level jet’s negative wind shear on the wind turbine, *Wind Energy Science* **2**, 533 (2017).
- [19] J. Wilczak, C. Finley, J. Freedman, J. Cline, L. Bianco, J. Olson, I. Djalalova, L. Sheridan, M. Ahlstrom, J. Manobianco, J. Zack, J. R. Carley, S. Benjamin, R. Coulter, L. K. Berg, J. Mirocha, K. Clawson, E. Natenberg, and M. Marquis, The wind forecast improvement project (WFIP): A public–private partnership addressing wind energy forecast needs, *Bull. Am. Meteorol. Soc.* **96**, 1699 (2015).
- [20] S. Frandsen, R. Barthelmie, S. Pryor, O. Rathmann, S. Larsen, J. Højstrup, and M. Thøgersen, Analytical modelling of wind speed deficit in large offshore wind farms, *Wind Energy* **9**, 39 (2006).
- [21] L. P. Chamorro, R. E. A. Arndt, and F. Sotiropoulos, Turbulent flow properties around a staggered wind farm, *Boundary-Layer Meteorol.* **141**, 349 (2011).
- [22] L. P. Chamorro and F. Porté-Agel, Turbulent flow inside and above a wind farm: a wind-tunnel study, *Energies* **4**, 1916 (2011).
- [23] M. Calaf, C. Meneveau, and J. Meyers, Large eddy simulations of fully developed wind-turbine array boundary layers, *Phys. Fluids* **22**, 015110 (2010).
- [24] R. B. Cal, J. Lebrón, L. Castillo, H. S. Kang, and C. Meneveau, Experimental study of the horizontally averaged flow structure in a model wind-turbine array boundary layer, *J. Renew. Sustain. Energy* **2**, 013106 (2010).
- [25] R. J. A. M. Stevens and C. Meneveau, Flow structure and turbulence in wind farms, *Annu. Rev. Fluid Mech.* **49**, 311 (2017).
- [26] M. Abkar and F. Porté-Agel, Influence of atmospheric stability on wind-turbine wakes: A large-eddy simulation study, *Phys. Fluids* **27**, 035104 (2015).
- [27] R. J. Barthelmie, M. J. Churchfield, P. J. Moriarty, J. K. Lundquist, G. S. Oxley, S. Hahn, and S. C. Pryor, The role of atmospheric stability/turbulence on wakes at the egmond aan zee offshore wind farm, *J. Phys. Conf. Ser.* **625**, 012002 (2015).
- [28] C.-H. Moeng, A large-eddy simulation model for the study of planetary boundary-layer turbulence, *J. Atmos. Sci.* **41**, 2052 (1984).
- [29] P. J. Mason and D. J. Thomson, Stochastic backscatter in large-eddy simulations of boundary layers, *J. Fluid Mech.* **242**, 51 (1992).

- [30] R. J. A. M. Stevens, J. Graham, and C. Meneveau, A concurrent precursor inflow method for large eddy simulations and applications to finite length wind farms, *Renewable Energy* **68**, 46 (2014).
- [31] J. Meyers and C. Meneveau, Large eddy simulations of large wind-turbine arrays in the atmospheric boundary layer, 48th AIAA Aerospace Sciences Meeting Including the New Horizons Forum and Aerospace Exposition AIAA 2010-827 4 - 7 January 2010, Orlando, Florida, AIAA 2010 (2010).
- [32] P. J. Mason, Large-eddy simulation of the convective atmospheric boundary layer, *J. Atmos. Sci.* **46**, 1492 (1989).
- [33] F. T. M. Nieuwstadt, P. J. Mason, C.-H. Moeng, and U. Schumann, *Turbulent Shear Flows 8* (Springer, Berlin, Heidelberg, 1993).
- [34] P. J. Mason and S. H. Derbyshire, Large eddy simulation of the stably-stratified atmospheric boundary layer, *Boundary-Layer Meteorol.* **53**, 117 (1990).
- [35] E. M. Saiki, C.-H. Moeng, and P. P. Sullivan, Large-eddy simulation of the stably stratified planetary boundary layer, *Boundary-Layer Meteorol.* **95**, 1 (2000).
- [36] B. Kosović and J. A. Curry, A large eddy simulation study of a quasi-steady stably stratified atmospheric boundary layer, *J. Atmos. Sci.* **57**, 1052 (2000).
- [37] L. Mahrt, Stably stratified atmospheric boundary layers, *Annu. Rev. Fluid Mech.* **46**, 23 (2014).
- [38] R. J. Beare, M. K. Macvean, A. A. M. Holtslag, J. Cuxart, I. Esau, J.-C. Golaz, M. A. Jimenez, M. Khairoutdinov, B. Kosovic, D. Lewellen, T. S. Lund, J. K. Lundquist, A. McCabe, A. F. Moene, Y. Noh, S. Raasch, and P. Sullivan, An intercomparison of large eddy simulations of the stable boundary layer, *Boundary-Layer Meteorol.* **118**, 247 (2006).
- [39] D. Allaerts and J. Meyers, Boundary-layer development and gravity waves in conventionally neutral wind farms, *J. Fluid Mech.* **814**, 95 (2017).
- [40] D. Allaerts and J. Meyers, Gravity waves and wind-farm efficiency in neutral and stable conditions, *Boundary-Layer Meteorol.* **166**, 269 (2018).
- [41] M. Dörenkämper, B. Witha, G. Steinfeld, D. Heinemann, and M. Kühn, The impact of stable atmospheric boundary layers on wind-turbine wakes within offshore wind farms, *J. Wind Eng. Ind. Aerodyn.* **144**, 146 (2015).
- [42] B. Witha, G. Steinfeld, M. Dörenkämper, and D. Heinemann, Large-eddy simulation of multiple wakes in offshore wind farms, *J. Phys. Conf. Ser.* **555**, 012108 (2014).
- [43] M. P. van der Laan and N. N. Sørensen, Why the Coriolis force turns a wind farm wake clockwise in the northern hemisphere, *Wind Energy Science* **2**, 285 (2017).
- [44] M. F. Howland, A. S. Ghate, and S. K. Lele, Influence of the geostrophic wind direction on the atmospheric boundary layer flow, *J. Fluid Mech.* **883**, A39 (2020).
- [45] M. Abkar and F. Porté-Agel, Influence of the Coriolis force on the structure and evolution of wind turbine wakes, *Phys. Rev. Fluids* **1**, 063701 (2016).
- [46] D. Allaerts and J. Meyers, Large eddy simulation of a large wind-turbine array in a conventionally neutral atmospheric boundary layer, *Phys. Fluids* **27**, 065108 (2015).
- [47] Y. T. Wu and F. Porté-Agel, Simulation of turbulent flow inside and above wind farms: Model validation and layout effects, *Boundary-Layer Meteorol.* **146**, 181 (2013).
- [48] H. Lu and F. Porté-Agel, Large-eddy simulation of a very large wind farm in a stable atmospheric boundary layer, *Phys. Fluids* **23**, 065101 (2011).
- [49] K. Bhaganagar and M. Debnath, The effects of mean atmospheric forcings of the stable atmospheric boundary layer on wind turbine wake, *J. Renew. Sustain. Energy* **7**, 013124 (2015).
- [50] M. Abkar, A. Sharifi, and F. Porté-Agel, Wake flow in a wind farm during a diurnal cycle, *J. Turb.* **625**, 012031 (2016).
- [51] V. Sharma, M. B. Parlange, and M. Calaf, Perturbations to the spatial and temporal characteristics of the diurnally-varying atmospheric boundary layer due to an extensive wind farm, *Boundary-Layer Meteorol.* **162**, 255 (2017).
- [52] A. C. Fitch, J. K. Lundquist, and J. B. Olson, Mesoscale influences of wind farms throughout a diurnal cycle, *Mon. Wea. Rev.* **141**, 2173 (2013).
- [53] J. S. Na, E. Koo, E. K. Jin, R. Linn, S. C. Ko, D. Muñoz-Esparza, and J. S. Lee, Large-eddy simulations of wind-farm wake characteristics associated with a low-level jet, *Wind Energy* **21**, 163 (2018).
- [54] J. D. Albertson and M. B. Parlange, Surface length-scales and shear stress: implications for land-atmosphere interaction over complex terrain, *Water Resour. Res.* **35**, 2121 (1999).
- [55] R. J. A. M. Stevens, D. F. Gayme, and C. Meneveau, Generalized coupled wake boundary layer model: applications and comparisons with field and LES data for two real wind farms, *Wind Energy* **19**, 2023 (2016).
- [56] M. Zhang, M. G. Arendshorst, and R. J. A. M. Stevens, Large eddy simulations of the effect of vertical staggering in extended wind farms, *Wind Energy* **22**, 189 (2019).
- [57] S. N. Gadde and R. J. A. M. Stevens, Effect of Coriolis force on a wind farm wake, *J. Phys. Conf. Ser.* **1256**, 012026 (2019).
- [58] J. D. Albertson, *Large Eddy Simulation of Land-Atmosphere Interaction*, Ph.D. thesis, University of California (1996).
- [59] Á. Jiménez, A. Crespo, and E. Migoya, Application of a LES technique to characterize the wake deflection of a wind turbine in yaw, *Wind Energy* **13**, 559 (2010).
- [60] M. Calaf, M. B. Parlange, and C. Meneveau, Large eddy simulation study of scalar transport in fully developed wind-turbine array boundary layers, *Phys. Fluids* **23**, 126603 (2011).
- [61] E. Bou-Zeid, C. Meneveau, and M. B. Parlange, A scale-dependent Lagrangian dynamic model for large eddy simulation of complex turbulent flows, *Phys. Fluids* **17**, 025105 (2005).
- [62] R. Stoll and F. Porté-Agel, Effects of roughness on surface boundary conditions for large-eddy simulation, *Boundary-Layer*

- Meteorol. **118**, 169 (2006).
- [63] R. Stoll and F. Porté-Agel, Large-eddy simulation of the stable atmospheric boundary layer using dynamic models with different averaging schemes, *Boundary-Layer Meteorol.* **126**, 1 (2008).
- [64] C. Canuto, Y. M. Hussaini, A. Quarteroni, and T. A. Zang, *Spectral Methods in Fluid Dynamics* (Springer, Netherlands, 1998).
- [65] J. H. Ferziger and M. Perić, *Computational methods for fluid dynamics* (Springer, 2002).
- [66] S. Basu and A. Lacser, A cautionary note on the use of monin–obukhov similarity theory in very high-resolution large-eddy simulations, *Boundary-Layer Meteorol.* **163**, 351 (2017).
- [67] J. B. Klemp and D. K. Lilly, Numerical simulation of hydrostatic mountain waves, *J. Atmos. Sci.* **68**, 46 (1978).
- [68] R. J. A. M. Stevens, D. F. Gayme, and C. Meneveau, Large eddy simulation studies of the effects of alignment and wind farm length, *J. Renew. Sustain. Energy* **6**, 023105 (2014).
- [69] A. Sescu and C. Meneveau, A control algorithm for statistically stationary large-eddy simulations of thermally stratified boundary layers, *Q. J. R. Meteorol. Soc.* **140**, 2017 (2014).
- [70] A. A. M. Holtslag and F. T. M. Nieuwstadt, Scaling the atmospheric boundary layer, *Boundary-Layer Meteorol.* **36**, 201 (1986).
- [71] L. F. Richardson, The supply of energy from and to atmospheric eddies, *Proc. R. Soc. Lond. A.* **97**, 354 (1920).
- [72] G. I. Taylor, Effect of variation in density on the stability of superposed streams of fluid, *Proc. R. Soc. Lond. A* **132**, 499 (1931).
- [73] J. Miles, Richardsons criterion for the stability of stratified shear flow, *Phys. Fluids* **29**, 3470 (1986).
- [74] B. Galperin, S. Sukoriansky, and P. S. Anderson, On the critical Richardson number in stably stratified turbulence, *Atmosph. Sci. Lett.* **8**, 65 (2007).
- [75] S. S. Zilitinkevich, T. Elperin, N. Kleerorin, I. Rogachevskii, I. Esau, T. Mauritsen, and M. W. Miles, Turbulence energetics in stably stratified geophysical flows: Strong and weak mixing regimes, *Q. J. R. Meteorol. Soc.* **134**, 793 (2008).
- [76] C. Meneveau, The top-down model of wind farm boundary layers and its applications, *J. Turb.* **13**, 1 (2012).
- [77] R. J. A. M. Stevens, Dependence of optimal wind-turbine spacing on wind-farm length, *Wind Energy* **19**, 651 (2016).
- [78] J. T. Rominger and H. M. Nepf, Flow adjustment and interior flow associated with a rectangular porous obstruction, *J. Fluid Mech.* **680**, 636 (2011).
- [79] J. C. R. Hunt and W. H. Snyder, Experiments on stably and neutrally stratified flow over a model three-dimensional hill, *J. Fluid Mech.* **96**, 671 (1980).
- [80] P. G. Baines, Observations of stratified flow over two-dimensional obstacles in fluid of finite depth, *Tellus* **31**, 351 (1979).
- [81] P. Sagaut, *Large eddy simulation for incompressible flows: an introduction* (Springer Science & Business Media, 2006).
- [82] K. S. Hansen, R. J. Barthelmie, L. E. Jensen, and A. Sommer, The impact of turbulence intensity and atmospheric stability on power deficits due to wind turbine wakes at Horns Rev wind farm, *Wind Energy* **15**, 183 (2012).
- [83] S. K. Shah and E. Bou-Zeid, Direct numerical simulations of turbulent Ekman layers with increasing static stability: Modifications to the bulk structure and second-order statistics, *J. Fluid Mech.* **760**, 494 (2014).
- [84] A. S. Monin and A. M. Yaglom, *Statistical fluid mechanics, vol. 1. mechanics of turbulence* (1971).
- [85] A. Segalini and J.-Å. Dahlberg, Blockage effects in wind farms, *Wind Energy* **23**, 120 (2020).
- [86] J. Bleeg, M. Purcell, R. Ruisi, and E. Traiger, Wind farm blockage and the consequences of neglecting its impact on energy production, *Energies* **11**, 1609 (2018).
- [87] K. L. Wu and F. Porté-Agel, Flow adjustment inside and around large finite-size wind farms, *Energies* **10**, 2164 (2017).